Characterization of High Performance Waveguide Coupled Silicon Germanium Avalanche Photodiodes

Olivier Carpentier

Master's Thesis

Department of Electrical & Computer Engineering

McGill University

Montreal,Quebec

November 16, 2020

A thesis submitted to McGill University in partial fulfillment of the requirements for the degree of Master of Engineering in Electrical Engineering

ABSTRACT

With ever increasing internet traffic, driven by the spread of streaming services and reliance on cloud infrastructure, there is a growing need for fast, energy efficient and affordable interconnects. One technology that is a good candidate to provide such interconnects is silicon photonics (SiP). This technology enables the use of silicon based devices to modulate and detect light in fiber optic communication, allowing for highly scalable production. With current standard communication speeds of 100 Gb/s and the current development of 400 Gb/s systems, SiP devices will need to perform at ever higher speeds to stay relevant with demand.

In this thesis, we perform a parametric study of silicon-germanium (SiGe) photodetectors (PD) to provide insight on the effect of multiple design parameters on the performance of such devices. We characterized over a hundred different devices by measuring parameters such as dark current, photocurrent, frequency response, gain and responsivity. We then present in greater details three different PD architectures. We report a vertical design capable of 28 Gbit/s error free operation with -9 dBm input power as well as a gain-bandwidth product > 400 without any digital signal processing (DSP) and a separate absorption-charge-multiplication (SACM) design with 25 Gb/s error free operation with -12 dBm input power without the use of any DSP. We also report 112 Gb/s pulse amplitude modulation (PAM)-4 operation below the KP4 forward error correction (FEC) threshold of 2.0×10^{-4} using the vertical P-I-N avalanche PD (APD) with -8dBm input power, which is to the best of our knowledge the highest reported bitrate using an APD on SiP platform.

ABRÉGÉ

La constante croissance de la demande d'accès à l'Internet, stimulée par le déploiement des services de *streaming* et de l'infrastructure infonuagique, crée un besoin croissant pour des connections rapide, énergétiquement efficaces et abordables. Une des technologies qui représente un bon candidat pour offrir de tels connections est la photonique sur silicium (SiP). Cette technologie permet l'utilisation de dispositifs à base de silicium pour moduler et détecter des signaux lumineux transmis par fibre optique, permettant ainsi une production à haut volume. Avec les standards établis atteignant des vitesses de 100 Gb/s et le développement de la prochaine génération d'interconnexions à 400 Gb/s, les dispositifs de SiP devront performer à des vitesses de plus en plus élevées pour rester compétitifs.

Au cours de cette thèse, nous performons une analyse paramétrique de photodétecteurs (PD) silicium-germanium (SiGe) pour fournir une meilleure compréhension de l'effet de différents paramètres de conception sur la performance des PD. Nous avons caractérisé plus d'une centaine de dispositifs en mesurant des paramètres tels que leur courant sombre, photocourant, réponse en fréquence, gain et responsivité. Nous présentons ensuite en plus de détails trois architectures de PD différentes. Nous présentons un arrangement vertical capable d'opérer à 28 Gbits/s sans erreurs avec -9 dBm de puissance à l'entrée ainsi qu'un produit gain-largeur-de-bande $>$ 400 Gb/s sans l'utilisation de traitement de signal numérique (DSP), ainsi qu'un arrangement de type séparation d'absorption-charge-multiplication (SACM) opérant sans erreurs à 25 Gb/s avec une puissance à l'entrée de -12 dBm sans l'utilisation de DSP. Nous

présentons également une structure P-I-N verticale à effet avalanche (APD) opérant sous la limite de correction d'erreur (FEC) de 2×10^{-4} à une vitesse de 112 Gb/s et un format de modulation d'amplitude du pulse (PAM)-4 avec -8 dBm de puissance à l'entrée, ce qui représente, à notre connaissance, le débit le plus élevé d'une APD sur la plateforme SiP.

ACKNOWLEDGEMENTS

I would like to thank my supervisor, Professor David Plant, for his continued guidance and support since the first day I joined his lab. David invested a lot of time and energy in me, allowing me to work with some of the best equipment in Canada, cutting edge technology and collaborate with dynamic partnerships. He provided me with a trully unique opportunity for which I am extremely grateful.

I also want to thank all my colleagues from the Photonic Systems Group, without which my thesis would not have been the same. I want to especially thank Alireza Samani for his mentorship. Ali has always been extremely generous of his time, spending nights in the lab to teach me the ropes, and always open for insightful discussions. I am grateful for his friendship and constant support throughout my thesis and I'll be sure to stay in touch. I would also like to thank Maxime Jacques, for his work ethic and high standards of quality which always pushed me to do better, as well as his wonderful sens of humor. Maxime has not only provided me with a constant supply of coffee, but also a sens of camaraderie that I hope will persist into the future. I finally want to thank Eslam El-Fiky, for the insightful discussions we had, his honesty and straight shooting attitude. Thank you all for your help and I hope we stay connected.

TABLE OF CONTENTS

LIST OF TABLES

LIST OF FIGURES

LIST OF ACRONYMS

APD Avalanche Photodiode.

BERT Bit Error Rate Tester.

BPG Bit Pattern Generator.

BW Bandwidth.

CMOS Complementary Metal-Oxide-Semiconductor.

DAC Digital-to-Analog Converter.

DC Direct Current.

DCA Digital Communication Analyzer.

DSP Digital Signal Processing.

EC Edge Coupler.

EHP Electron-Hole Pair.

FAU Fiber Array Unit.

GC Grating Coupler.

GSG Ground-Signal-Ground.

IC Integrated Circuits.

LCA Lightwave Component Analyzer.

OOK On-Off Keying.

PAM Pulse Amplitude Modulation.

PIC Photonic Integrated Circuit.

PRBS Pseudorandom Binary Sequence.

RF Radio Frequency.

ROSA Receiver Optical Sub-Assembly.

SACM Separate Absorption-Charge-Multiplication.

SEM Scanning Electron Microscope.

SiP Silicon Photonics.

SWG Sub-Wavelength Grating.

WDM Wavelength Division Multiplexing.

CHAPTER 1
Introduction to silicon photonics

1.1 The Need for Optical Interconnects

Over the last few years, the demand for Internet traffic has been growing exponentially. With the increase of big drivers of data traffic such as streaming services, social media and cloud computing, there is a growing pressure for our global infrastructure to evolve and support the needs of the future. In numbers, global data center traffic is expected to grow at a compound annual growth rate (CAGR) of 25% until 2024 [2] with only 15% of the traffic being exchanged with the end user [3]. That means 20 zettabytes by 2021, which could grow to over 60 zettabytes by 2025. Meanwhile, the bulk of all this data traffic currently stays within the data center (71.5%) or goes from one data center to another (13.6%), and this fraction is expected to grow even further.

This trend puts enormous pressure on data center operators to upgrade their interconnect infrastructure to accommodate this growing traffic. While optical interconnects offer much higher data transfer rate with longer reach than their copper counterparts, their cost is also significantly higher. One attractive technology to fulfill the need for high performance optical interconnect at an affordable cost is silicon photonics. The silicon photonics platform leverages established infrastructure of the

complementary metal-oxide-semiconductor (CMOS) industry to provide good optical performance with the high yield traditionally associated with silicon integrated circuits (IC).

Silicon photonics has received a lot of attention over the last three decades and now compares well with more traditional platforms such as indium phosphide on multiple levels. High performance active devices have been demonstrated on silicon, such as modulators and photodetectors, as well as passive devices such as waveguides, multiplexers, polarization splitter and rotators. The following section takes a look at the evolution of silicon photonics from its inception until today.

1.2 Silicon Photonics and Photodetectors

SiP technologies have received significant research attention for more than three decades. A seminal paper published in 1987 by Soref and Bennett [4] showed the possibility of using electric fields to change the carrier concentration in silicon and thus change the refractive index, paving the way for active photonics devices such as modulators. However, light detection using germanium photodetectors was already studied in the 1960s [5]. Even though optoelectronic integrated circuits were proposed by Soref in the 1980s, there was little progress in truly integrated silicon photonics until the early 2000s [6]. It is then that integrated SiP devices really started to compete with III-V equivalents, such as InP/InGaAsP devices.

In the late 2000s, Kang published a paper showing that germanium silicon avalanche photodiodes could perform on par with InP devices [7]. It showed a gain-bandwidth product, an important figure of merit for photodetectors, of 340 GHz, matching the best InP devices at the time. This top illuminated APD had a

separate absorption, charge and multiplication (SACM) structure. The novel contribution was the monolithic growth of the germanium layer on silicon. Previously, high performance Ge/Si PDs were made with wafer bonding technique, as the 4% lattice mismatch between Ge and Si would cause a high dislocation density and thus elevated dark current. However, through careful processing, it was shown that it is possible to produce a very sensitive monolithically grown APD.

To enable the next generation of transceivers, even higher bandwidth and sensitivity will be required. Some highly sensitive Si-Ge APDs [8] with operation parameters such as error-free at 25 Gb/s with only -12 dBm input power [9], 10 Gb/s with -29.5 dBm power [10] or 50 Gb/s PAM4 at -16 dBm sensitivity with a 2.4×10^{-4} bit-error-rate [11] have been shown. Some groups have shown photodetectors operating at high frequencies, with bandwidths in excess of 70 GHz [12, 13].

Another key benefit of silicon photonics is its CMOS compatibility. It is therefore possible to build monolithically integrated circuits that incorporate electrical components as well as optical components. The use of photodetectors and infrared light as a way to transmit data within a microprocessor (on-chip) was initially proposed by Goodman in 1984 [14], but only started to be considered as a practical solution around 2005 [15]. In the 2010s, some groups began to seriously study the use of silicon-germanium photodetectors for such applications [16–18]. In 2015, a group from Berkeley published a demonstration of a system with 70 million transistors and 850 photonic components. The resources of this microprocessor were split on two main regions of the chip: one region containing the 1 MB of memory, and the other with the RISC-V processor, able to run a modern instruction set [19].

Leading manufacturers are also gaining interest in silicon photonics-based products for datacom applications. This pushes the development of SiGe APDs to match the requirement for the transmission standards of today and tomorrow. Currently, optical transceivers for data center operations are built to match standards such as 400BASE-DR4 established by the IEEE 802.3 Working Group [20]. These standards are currently pushing modulation formats such as PAM4, carrying over 100 Gb/s per lane. Current literature shows that silicon photonics enables transceivers to operate at 400 Gb/s speeds with high bandwidth density and energy efficiency, using photodetectors with 35 GHz bandwidth and 0.9 A/W sensitivity in O-band [21].

1.3 Contribution and Thesis Outline

In recent years, there has been many theoretical studies to optimize the performance of silicon-germanium photodetectors through simulation work [22, 23]. However, there has not yet been a large scale parametric study of actual devices.

Over the course of my Master's research, I worked on characterizing over a hundred design variations of SiGe APDs. These devices were designed by graduate students that came before me, as the process from design and fabrication to receiving a piece of silicon wafer can take well over a year. I will therefore go over the key steps required for the design of such devices and highlight the key results from my measurements that effect the performance of SiGe APDs before presenting the best in class results that were achieved.

This thesis is organized in 5 chapters. This first chapter provided the context to the research topic and lays out the structure of the following chapters.

Chapter 2 goes over the basic knowledge of silicon photonics devices, both passive and active, required to understand the context in which SiGe APDs play their role. It then goes into more details regarding the considerations and trade-offs of APD design.

Chapter 3 outlines the multiple steps to characterize the performance of an APD, including calibration, dark current and photocurrent, small signal response and signal transmission performance. It also lays out the physical configuration to facilitate reproduction of these measurements.

Chapter 4 presents the most interesting findings for two types of application requirements: high gain-bandwidth product reaching 400 GHz and high data-rates reaching 112 Gb/s.

Chapter 6 summarizes the conclusions that can be drawn from the research and outlines future steps that can be taken to advance the topic further.

CHAPTER 2
Device Design Principles

In this chapter we outline the important design characteristics and functioning principles of passive and active silicon photonic devices. The most important components required to make a SiP receiver will be covered on a high level, before focusing in to the photodiode. In the following chapter, we will simulate the performance of these devices.

2.1 Passive components

Passive components are a category of components that only deal with light, while active components also include electrical signals. Here we present two types of passive components: waveguides, which propagate light within the chip, and couplers, which couple light from and to the outside of the silicon wafer.

2.1.1 Waveguides

Silicon waveguides follow the same principle as any waveguide. By using mediums of different refractive index, we construct a path for light to propagate. Figure 2–1 shows the cross section of a few different types of commonly used waveguides.

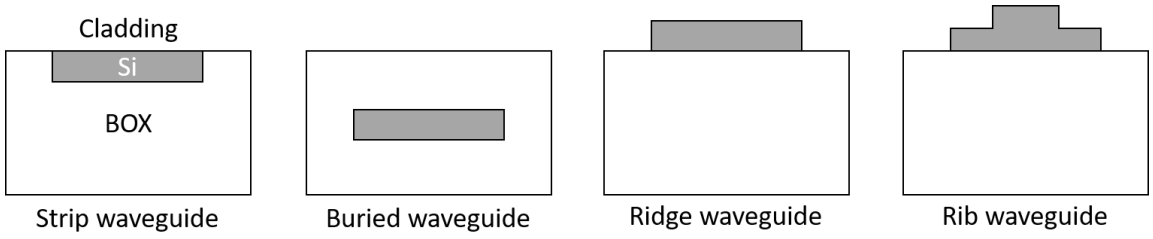

Figure 2–1: Cross section of different silicon waveguides.

The key relation to determine weather a certain wave will propagate through the waveguide is the dispersion relation, or $b-V$ curve. For TE modes in symmetric waveguides, the normalized dispersion relation is as follows:

$$\tan\left(V\sqrt{1-b}-\frac{m\pi}{2}\right)=\frac{\sqrt{b}}{\sqrt{1-b}} \tag{2.1}$$

where the propagation constant b is defined as

$$b=\frac{n_{eff}^2-n_2^2}{n_1^2-n_2^2} \tag{2.2}$$

The refractive index n_1 is the core and n_2 the cladding. By analyzing the dispersion relation, we can restrain the waveguide dimensions to support a single mode. Figure 2–2 shows the typical dispersion relation for TE mode in a slab waveguide. To keep $V<\pi$ and ensure that we only support a single mode we use the following relation between V, waveguide size, refractive index and wavelengths:

$$V=k_0 w\sqrt{n_1^2-n_2^2} \tag{2.3}$$

where $k_0=2\pi/\lambda_0$ is the wavenumber and w the full width of the waveguide. Of course, these operations need to be carried out for TM modes as well, however these

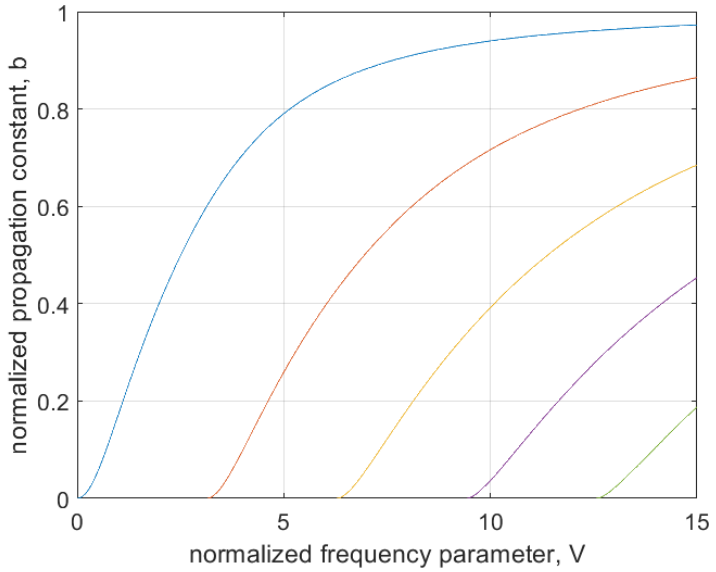

Figure 2–2: b-V curves for TE modes of a dielectric slab waveguide.

will not be included for brevity. With standard SOI process using a 220 nm top silicon layer, we often use a 500 × 220 nm strip waveguide [24].

2.1.2 Grating couplers and edge couplers

In order to coupe light to a silicon wafer, we need to use one of two special structures: grating couplers or edge couplers. Grating couplers (GC) are a sub-wavelength grating (SWG) that couple incident light that is perpendicular to the plane of the wafer into the waveguides. Edge couplers (EC) are simpler structures that compress or expand the mode of incident light that is in plane with the waveguides.

Grating couplers. GCs act like any other grating: they diffract the incident light. On a high level, we can see these gratings as modifying the incident light's wavevector $\vec{k}$. Under the right conditions, a fraction of the incident light with the

right wavevector will be able to couple with the waveguide's supported mode. A GC can be designed to couple with TE or TM light, but not both simultaneously.

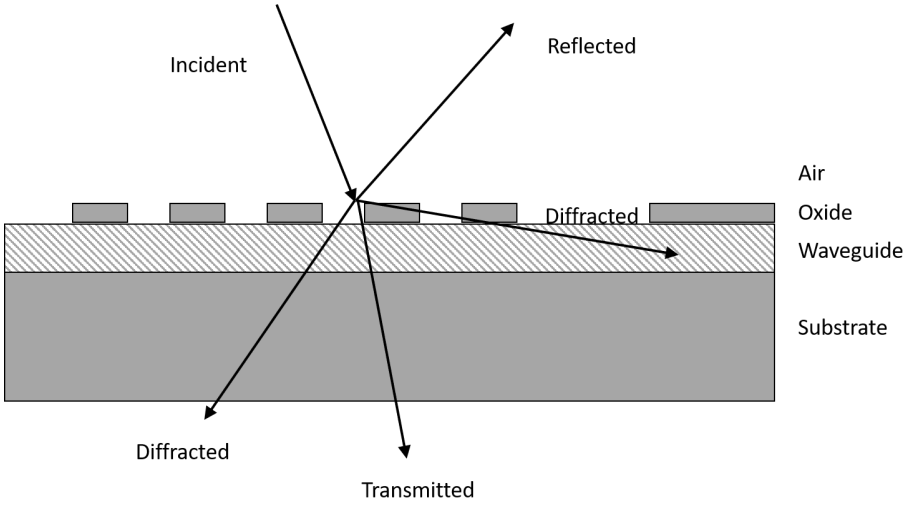

Figure 2–3: Cross section of a grating coupler.

They are extremely useful for testing purpose for 2 main reasons: ease of alignment and die level testing. A GC can have a relatively large area, easily of 30 μm $\times$ 30 μm, allowing a user to manually position a FAU to couple light to a DUT. Furthermore, GCs do not require complex dicing. Multiple designs can be placed onto a die, and each one can be subsequently tested without the need to dice each region to expose functional areas in the middle of the die. This allows testing on a die level to be conducted much faster, and even with some level of automation. Section 3.2.1 discusses the specific layout used for testing purposes.

Edge couplers. ECs generally have lower insertion loss than GCs, have a broadband response and couple both TE and TM modes, but require a more precise alignment. For this reason, ECs are most commonly used at later stages of prototyping and in finished products.

Figure 2–4 shows SEM images of EC structures. In the larger view, we can see the tape used to secure the chip in the SEM, the cross section of the entire SOI wafer, as well as the precise cut that was made to create a recessed area for the edge coupler facets. Figure 2–4a shows this large cross section with an array of ECs that can interface with an FAU. Just like with GCs, there is a pair of EC that is connected back-to-back to allow precise alignment of the FAU. This configuration is suitable for photonic integrated circuits (PICs) such as a receiver optical sub-assembly (ROSA). Figure 2–4b shows the end of a single EC. We can see in the center the oxide cladding of the rib waveguide that goes to the edge of the chip. With careful observation, we can even discern the outline of the nano-taper within the oxide.

2.1.3 Multiplexers

Multiplexers and demultiplexers are an important component of communication systems. These structures allow to combine or separate multiple wavelengths in a single waveguide. For example, a single fiber could carry multiple signals at different frequencies. Once on-chip, this light will be separated the various wavelengths λ_0, λ_1,... λ_n into different channels that will all be detected independently. This technique is called wavelength division multiplexing (WDM) and is used in high bandwidth applications. However, multiplexers are a complex topic onto themselves and will not be covered here.

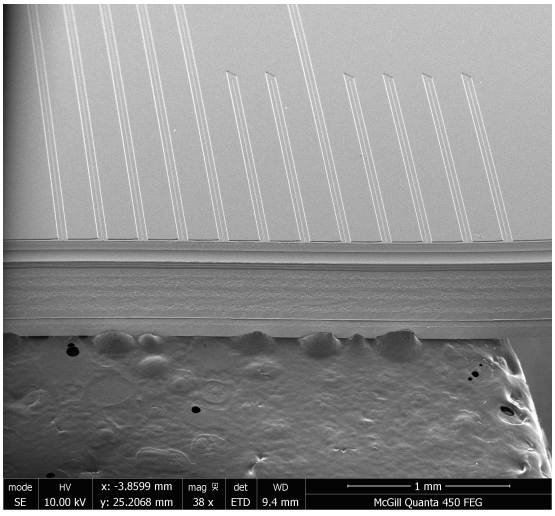

(a) EC array.

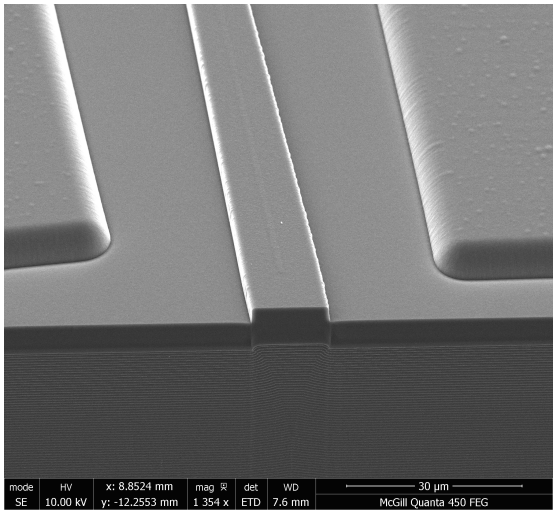

(b) Single EC.

Figure 2–4: SEM view of ECs on a silicon wafer.

2.2 Active components

Active components have an electrical input or output as well as an optical one. Although multiple active components are important in silicon photonics, such as modulators, we focus here on photodetectors. They are complex devices with multiple design components that need to be carefully considered. We will go over some basic theory of semiconductor junctions, then include some of the more complex components oh high performance photodiode design.

2.2.1 Photodiodes

Photodetectors are essentially p-n junctions. Although simple in their most basic form, much design effort is needed to achieve the performances that we see today in commercial-grade photodiodes or research papers.

Here, we outline some fundamental principles of operation of photodiodes as well as design considerations for high performance devices.

Photodetection occurs because we use a semiconductor which has an electronic structure that is sensitive to the photon energy range used in telecommunication. When hit by a photon, an electron from the semiconductor will move from its low energy state to an excited state, provided the photon has enough energy to breach the band gap. This excited electron is now a free carrier and is able to be collected by nearby electrodes, thus generating a current.

For photodetection to occur, a few conditions have to be met. First, the photon energy has to be larger than the bandgap of the material for the electron to generate an electron-hole pair (EHP). Second is carrier collection. The absorption process generates a free carrier carrier which also needs an adequately long lifetime τ and the geometry of the device needs to be appropriate to collect this carrier. Otherwise, it will recombine with a hole and the carrier is lost, therefore not contributing to the photocurrent. And third, the noise floor of the device has to be sufficiently low for the photogenerated carriers to have a measurable impact on the total current.

Bandgap. Lasers used in telecommunication often operate in two wavelength ranges: O-band, which ranges from 1260 nm to 1360 nm, and C-band, which ranges from 1530 nm to 1565 nm. For silicon photonics, this means that we can't use silicon as a photodetector, as the bandgap for silicon is roughly 1.1 eV or 1130 nm. Essentially, silicon is transparent to light with longer wavelength. However, germanium, also a column IV semiconductor and CMOS compatible material, has a bandgap of around 0.67 eV or 1850 nm. Figure 2–5 shows the absorption coefficient of some common semiconductors used in photodetectors.

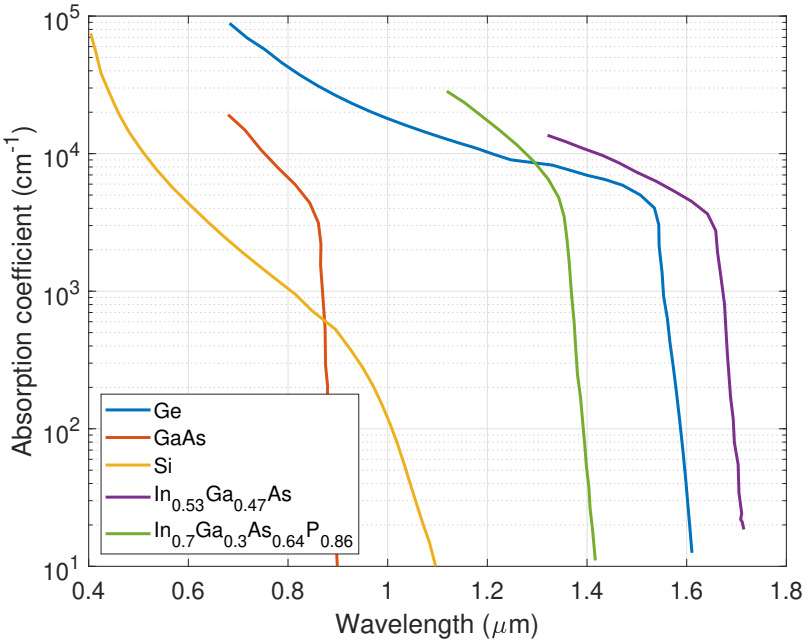

Figure 2–5: Absorption profile of a few common semiconductor materials [1].

These properties allow us to design waveguides in silicon with relatively low absorption and photodetectors where light is absorbed in germanium and the free carriers are conducted through the silicon. Even though the absorption coefficient of bulk Ge drops sharply after 1550 nm, it is possible to make the absorption region long enough to capture enough incident light. Furthermore, there are techniques to extend the absorption of Ge, such as exploiting indirect transitions [25].

Carrier collection. Carrier collection is an important part of photodetector design and is affected by material property as well as device geometry. There are two mechanisms by which carriers move within the semiconductor material: drift and diffusion. Diffusion occurs through the random movement of carriers through the lattice, while drift occurs when an electric potential applies a force on the carrier,

causing motion. In photodetectors, we are mostly concerned by EHP that are optically generated in such a way that the resulting carriers will drift to our electrodes to be collected. Because the electric field is mostly present in the depletion region, optically induced current will come from EHP generated in the diffusion region, and also from EHP generated in the n or p regions within a diffusion length $L_{p,n}$ of the depletion region.

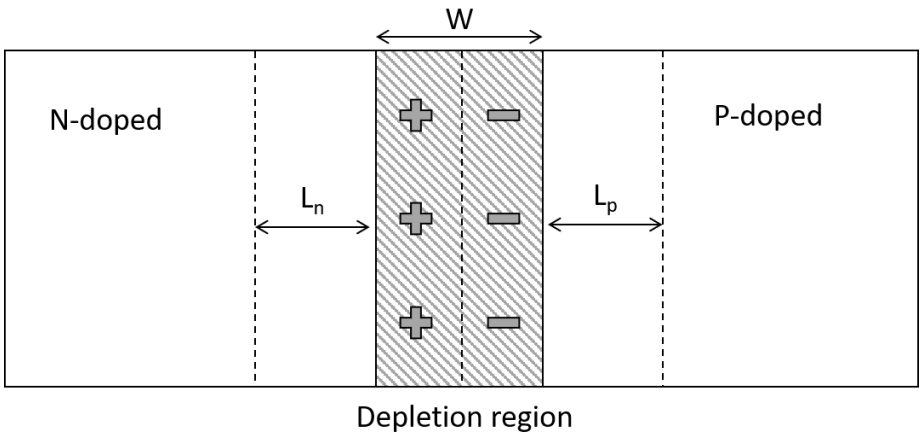

Figure 2–6: Cross section of a pn junction.

For a junction of area A and a rate of optical generation g_{op} in EHP/cm^{3}s, we can express the optically generated current as

$$I_{op} = qAg_{op}(L_p + L_n + W) \tag{2.4}$$

where q is the elemental charge and W is the width of the depletion region. Although having a larger area and a larger depletion region might help increase the total current, another factor needs to be considered carefully: response time. Indeed when the photodiode receives a short pulse of light, we are concerned by the time

needed to collect the associated current impulse. Some factors such as the transit time, RC constant and diffusion time need to be considered. Transit time depends on the length of the depletion region. The longer the region, the more distance a carrier has to travel before being collected. The time will be $W/v_{e,h}$ where $v_{e,h}$ is the velocity of electrons or holes in the transit region. The mean drift velocity being given by the mobility $\mu_{e,h}$ and the electric field E by the following relation:

$$v_{e,h} = \mu_{e,h} E \tag{2.5}$$

By varying the length of the depletion region, we also affect the junction capacitance C_j, which is given by

$$C_j = \epsilon A \left[\frac{q}{2\epsilon(V_0 - V)} \frac{N_d N_a}{N_d + N_a} \right] = \frac{\epsilon A}{W} \tag{2.6}$$

where ϵ is the permittivity, A is the area of the junction, q is the elementary charge, V_0 is the junction potential, V is the applied bias and $N_{a,d}$ are the acceptor and donor concentration, respectively. The expression in brackets is also the inverse of the equation for the length of the depletion region W. Rewriting the equation with W essentially gives the equation for a capacitor. Keeping the developed form of W, this equation clearly shows the relationship between physical constants, such as doping which affects $N_{a,d}$, and the capacitance.

There is also the contribution from diffusion, whose duration is limited by the carriers lifetime $\tau_{e,h}$. The more time a carrier takes before diffusing in the depletion region, the longer the response time to an optical impulsion becomes.

We now start to see the picture of the trade-offs required during the design process. A common design is the *p*-*i*-*n* photodiode. By placing an intrinsic or lightly doped region between the p and n regions, the depletion region covers the intrinsic region. If the absorption happens in this region, we can insure that the carriers will be swept by the electric field. By increasing the size of the depletion region, we can capture more light while decreasing the capacitance, thus the RC constant, but we also increase the transit time.

One additional component that is much harder to model through analytical expressions are the imperfections of the fabrication process. As we are dealing with heterostructures composed of semiconductors, such as silicon and germanium, as well as metals for the vias, many other considerations arise. Dislocations and imperfections in the lattice reduce carrier lifetime, and absorption of evanescent light by the vias reduce the efficiency of the device.

2.2.2 Avalanche photodiodes

Some photodiodes can be operated under a certain rage of reverse bias where the kinetic energy accumulated by the free carriers while they drift in the depletion region becomes high enough to excite other free carriers during collisions with the lattice, also called impact ionization. This mechanism is called the avalanche effect, as a small input gets amplified to a much larger signal. Once a free carrier impacts the lattice and generates another EHP, this new carrier can itself generate another EHP, and so on. The generation of multiple carriers from a single initial carrier is also called carrier multiplication, and is represented by the parameter M. Another

important parameter of avalanche photodiodes (APD) is the ionization ratio, or k-factor given by

$$k_A = \frac{\alpha_h}{\alpha_e} \tag{2.7}$$

where the ionization coefficients $\alpha_{e,h}$ represent the ionization probability per unit length for electrons and holes, respectively. Their inverse then gives the average distance traveled between ionization events. The k factor is important in determining the noise and response time of an APD as will be discussed later.

2.2.3 Heterojunction and metal-semiconductor junctions

A photodiode is a complex structure with multiple interfaces, from homojunctions where silicon meets silicon of a different doping concentration, to heterojunctions where silicon meets germanium and even metal-semiconductor junctions where silicon or germanium meets metal vias.

For metal-semiconductor interfaces, we want to avoid Schottky barriers which would hinder the flow of current. To obtain Ohmic contacts, we will place heavily doped semiconductors in contact with the metal vias. This will allow an accumulation of majority carriers at the interface or will create a small enough depletion region for the carriers to be able to tunnel through it.

In semiconductor-semiconductor junctions, in our case where Si and Ge meet, even though there might not be significant lattice mismatch as discussed in section 1.2, we still expect a discontinuity in the Fermi energy levels of the two semiconductors. A careful physical examination of the interface can shed some light on

the energy band discontinuities [26], and this influence of this interface should be considered in the design of a PD.

2.2.4 Sources of noise

There are multiple factors that contribute to noise in a photodiode, namely thermal noise, shot noise and excess or multiplication noise.

Thermal noise. Thermal noise, or dark-current noise, refers to the current measured in the absence of light. Due to thermal energy, EHPs can be generated randomly within the bulk material. When generated in the depletion region or within a diffusion length of the depletion region, these thermal generated EHP contribute to the measured current and can be amplified through the avalanche effect just like any photogenerated EHP. Dark current can be especially problematic in SiGe photodetectors due to the lattice mismatch and dislocations that can happen at the Si-Ge interface. However, when Ge is grown carefully, it is still possible to achieve low values of dark current [27].

Shot noise. Shot noise stems from the discrete nature of light. Although there may be a constant optical input power to the photodetector, the statistical distribution of incident photons will not be uniform, thus creating noise. The resulting current pulse of each EHP generation can also vary in length, thus adding to the noise.

Excess noise. Excess noise is related to shot noise, but is a bi-product of the avalanche effect, thus only observed in APDs. The excess noise factor, F_A, represents the increase in shot noise due to an imperfect multiplier. In principle, we would like the APD to amplify the signal through the impact ionization of only one

type of carrier. However, this is not the case in a practical device. Equation (2.8) defines excess noise factor where M is the multiplication factor and k_A is the impact ionization factor presented in eq. (2.7).

$$F_A(M) = k_A M + (1 - k_A)(2 - \frac{1}{M}) \tag{2.8}$$

If $k_A \rightarrow 0$, then the APD tends towards an ideal multiplicator. However, if $k_A \rightarrow 1$, then the amplification process takes longer and longer, as each type of carrier will also cause an impact ionization as it drifts through the high intensity E-field of the depletion region. This k-factor is dependent on the material, and some materials are better suited for multiplication than others. Germanium, the material used to absorb light in SiP, has a very high k-factor between 0.9 and 1.0, which leads to high multiplication noise. This happens to be also much higher than other traditional semiconductors such as GaAs ($0.45 \leq k \leq 0.55$) or InP ($0.35 \leq k \leq 0.45$). However, Si is one of the semiconductors with the lowest k-factor, between 0.0 and 0.1, and thus a good medium for multiplication [28].

CHAPTER 3
Testing and results

This chapter will go in depth in covering the measurement procedures used to reliably characterize an APD and will go in depth in the performance characteristics of a few designs. During this chapter and the following, some specifications will be omitted as the exact design parameters are under intellectual property protection with the industrial partner who enabled much of this research.

3.1 Design variations

Multiple design variations were evaluated, fabricated and tested. The main categories of PD design are presented in figure 3–1. For all design types, the waveguide conducting light to the PD is tapered and connects to the intrinsic germanium section where light will be absorbed. There, EHP are generated and extracted through the anode and cathode. As can be seen, metal vias make contact to heavily doped regions to allow for an Ohmic connection. The SLPIN and GeSLPIN designs are presented in subfigures 3–1a and 3–1b. Both are considered lateral PDs as most of the carrier travel within the semiconductor material is in plane. In the SLPIN design, carriers must drift from the germanium layer to the silicon before being extracted, while in the GeSLPIN design, the electrodes are connected directly to the germanium layer.

Vertical PDs, or VPIN, are presented in subfigures 3–1c and 3–1d. In this configuration, carriers travel mostly perpendicular to the plane of the device. The

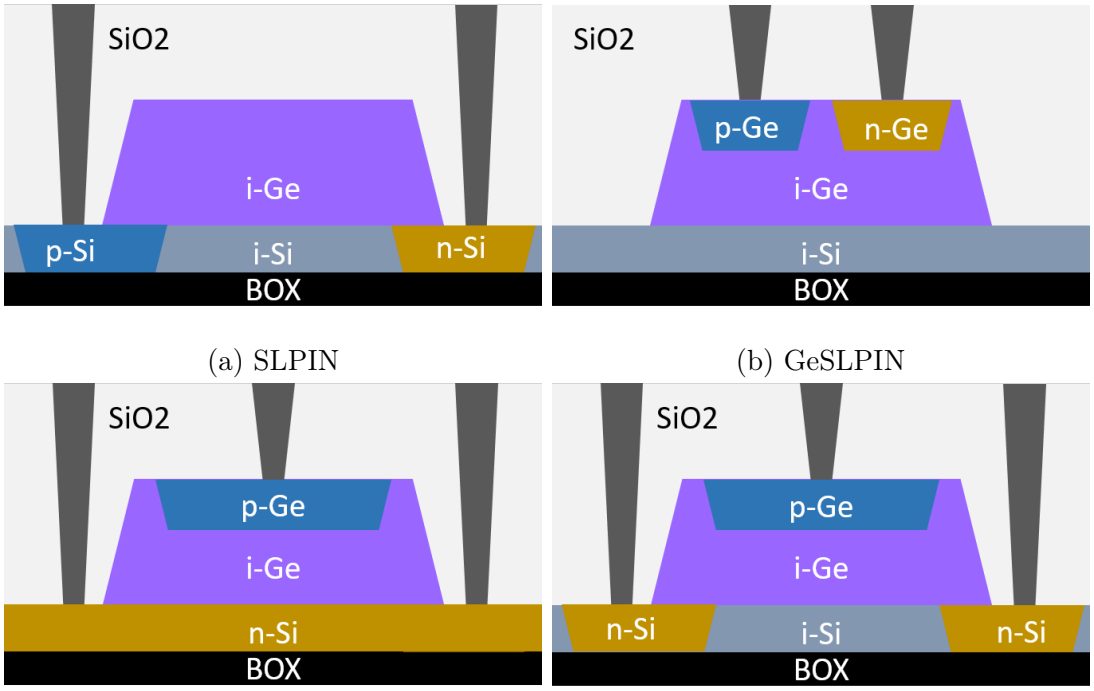

(a) SLPIN (b) GeSLPIN

(c) VPIN (d) SVPIN

Figure 3–1: Cross section of vertical and lateral PD designs.

anodes connects directly to the germanium while the cathodes connect to the silicon underneath it. Both cross sections shown are very similar, although one shows a width of intrinsic silicon under the germanium layer while the other shows strictly doped silicon. Adding intrinsic silicon under the germanium shifts the depletion layer in silicon to the intrinsic/n-doped interface. This leads to a higher potential drop within silicon, favoring multiplication to happen in Si.

There is also another design type called separate absorption, charge and multiplication (SACM). In this design shown in figure 3–2, the PIN structure is created within the silicon layer, while the germanium layer is mostly intrinsic, with a p-doped

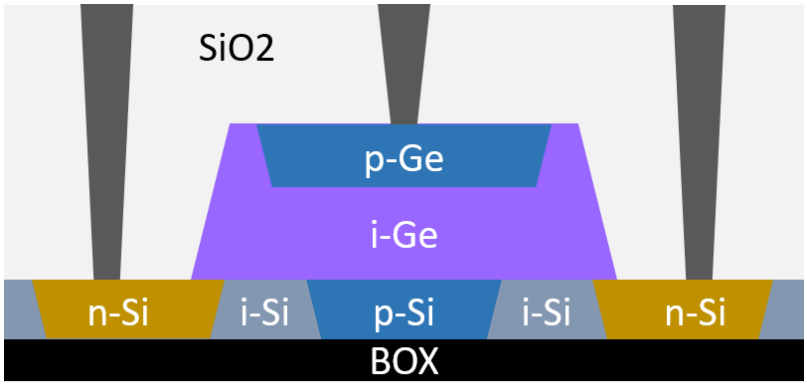

Figure 3–2: Cross section of SACM PD design.

region allowing an Ohmic contact with the vias. This configuration allows a careful control of the E-field, creating different regions for absorption and multiplication [29].

An important design parameter that was varied in the fabricated PDs is the height of the germanium layer. Two germanium heights were used: 200 nm, referred to as thin germanium layer, and 400 nm, the normal germanium process. This parameter is very important as it affects absorption, transit time and capacitance of the PD.

As a note, one of the design goals is to increase the device bandwidth. A critical design element is therefore to minimise the drift and diffusion time of minority carriers across the depletion region. In all the PD types presented, carriers travel perpendicular to the plane of light propagation, which goes through the cross sections shown. This allows the absorption region to be made quite long, therefore improving sensitivity while keeping transit times short.

3.2 Testing procedure

In this section we outline the various steps required to fully characterize the performance of a photodiode. Each of these steps were performed for at least some design variations.

3.2.1 Laboratory setup

To facilitate testing, the same layout template is used for every different PD. This allows the test and measurement equipment to interface in the same way with every PD. Figure 3–3 shows this standard layout.

To couple light to the GCs, we use a fiber array unit (FAU), essentially a glass prism with waveguides at a fixed pitch, each connected to an optical fiber. This FAU allows us to easily interface equipment such as lasers and power meters while offering a small and consistent footprint.

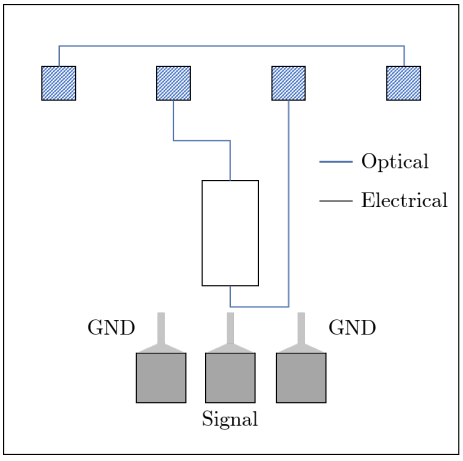

Figure 3–3: Standard design cell comprising 4 GCs (top), a PD (center), and 3 electrical pads (bottom) as well as traces and waveguides. Electrical routing was left open for visual clarity.

We also have three electrical pads where we can land DC or RF probes. The standard configuration is ground-signal-ground (GSG). Different designs will then route the metal traces differently to the PD. Figure 3–4 shows both an RF probe and an FAU interfacing with a PD.

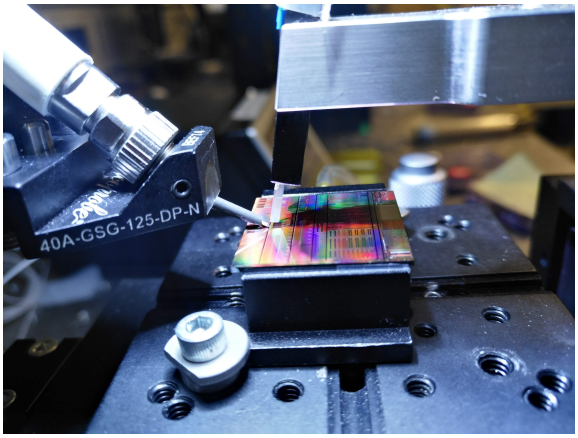

Figure 3–4: Electrical probe (left) and FAU (right) interfacing with a PD on a vacuum stage.

3.2.2 DC characterization

We initially measure the performance of a PD under direct current (DC). To do so, at least three distinct measurements need to be performed: grating coupler (GC) or edge coupler (EC) characterization, dark current and photocurrent.

The first step is to characterize the loss caused by the input and output ports to the PD. Generally, PDs are coupled to GC for testing purposes and EC for products, as was explained in section 2.1.2. This measurement is made possible by a pair of back-to-back GC that is included with every PD. These are the leftmost and rightmost GC in figure 3–3, directly connected by a waveguide. By aligning the fiber array with the back-to-back couplers, we can characterize the insertion loss of

the measurement and estimate the optical power that will reach the PD through the middle GCs. Figure 3–5 shows the typical transmission pattern for a back-to-back grating coupler with 0 dBm input power. Optimal transmission is centered around 1550 nm and decays exponentially as we move away in wavelengths. A different grating coupler is designed for O-band to have peak transmission around 1310 nm. This figure shows that each grating coupler has roughly a 5 dB insertion loss. Depending on the testing setup and individual GCs, insertion loss can get down to 3.5 dB in the best cases.

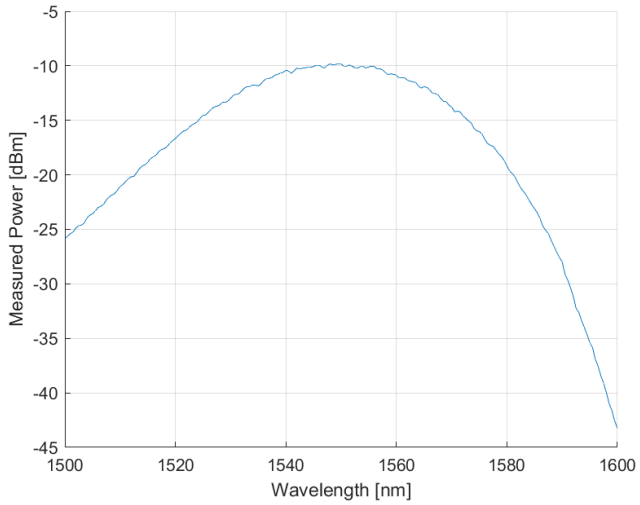

Figure 3–5: Typical transmission spectrum for back-to-back GCs.

The second step is dark current measurement. The electrical probe is landed on the GSG pads and the laser source is turned off. With a picoammeter, the current is precisely measured through a range of reverse biases that covers from 0 V to the start of the multiplication process. It is important that the current measurement be very precise, as dark currents can be lower than 1 nA. As figure 3–6 shows, dark

current increases gradually but as we increase bias the field becomes strong enough to cause multiplication.

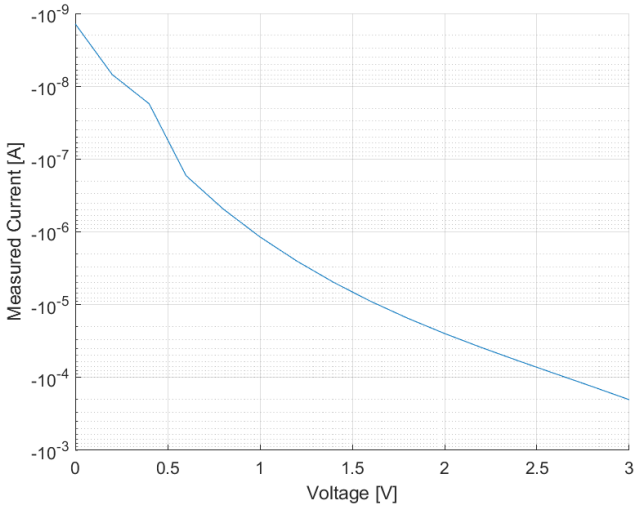

Figure 3–6: Sample dark current measurement.

Finally, the laser source is turned back on, and the laser output fiber is connected to one of the middle gratings to inject light in the PD. By changing the fiber connections without moving the fiber array itself, we are able to keep the alignment that we measured during the first step. At this stage, we are able to sweep multiple parameters: reverse bias, wavelength and optical power. Currents under illumination can range from the hundred μA range to the mA range. Considering that dark currents can be in the nA range, the test and measurement equipment must be able to cover over 6 orders of magnitude in current measurement. Reverse bias ranges typically from 0V to 4-6V, but in some cases can be over 10V. The light source also needs a wide tunable band. Measurements were performed over both O-band and

C-band wavelengths, typically ranging form 1260 nm - 1360 nm and 1530 nm - 1565 nm, respectively.

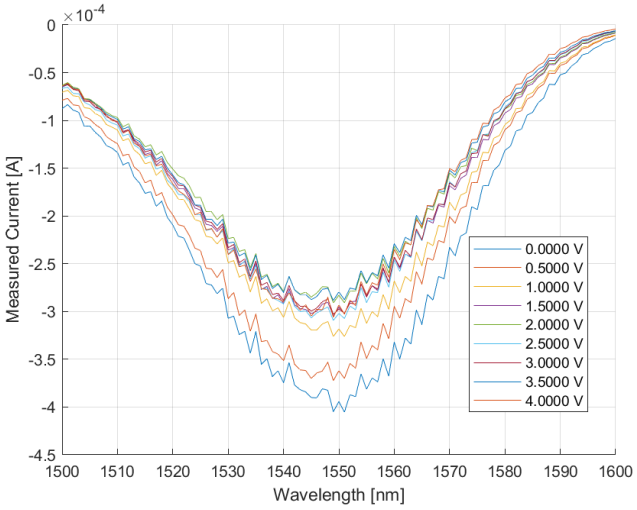

Figure 3–7: APD current over extended C-band for multiple bias points.

Figure 3–7 shows the current measured across wavelengths on a single PD for different bias points across the C-band. We can see the envelope caused by the GC transmission profile as shown in figure 3–5, as well as the offset caused by the dark current, which is constant across wavelengths. The current increases slightly at first as we start to apply a reverse bias, stabilizes and then increases rapidly as we enter multiplication. By only taking the points measured at 1550, or fixing the wavelength and only sweeping the bias, we obtain an I-V curve similar to figure 3–8 which shows the total current measured from the PD as well as the different operation regimes. For measurements in the O-band, the center wavelength would be 1310 nm.

The transmission GC, meaning the port through which light that is not absorbed by the PD would exit, was also monitored during IV measurements. However, we

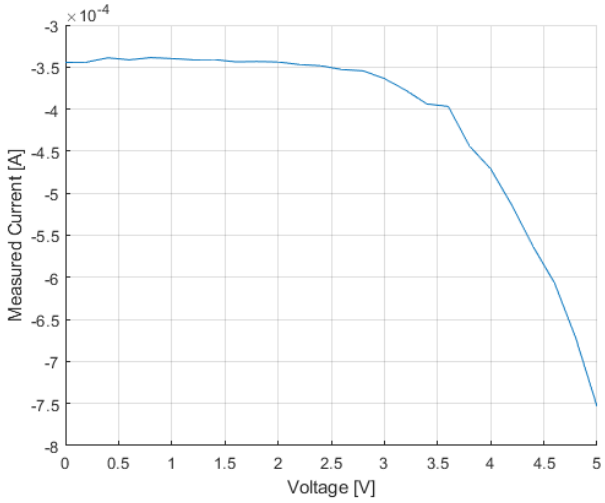

Figure 3–8: Sample I-V curve at 1550 nm.

found that, with standard *Ge* thickness, the signal was below our instrument's noise floor (less than −65 dBm) for our standard length of 15 μm, both in O and C band. However, for the thin Ge configurations of the same length operating in C band, we saw between −35 dBm and −25 dBm received through the exit port. This means that in some cases, up to −10 dB of the light reaching the PD was not absorbed. Hence, by increasing the absorption region of thin Ge devices designed for C band applications, slightly better responsivity might be reached.

3.2.3 Small signal

Small signal measurements are used to determined the bandwidth of the PDs. Our equipment allows us to test the opto-electrical bandwidth up to 50 GHz. A wideband optical signal is applied to the PD and a highly sensitive RF probe monitors the output signal. By doing so, we obtain the S-parameters of our device. We are particularly concerned with the real part of the S21 parameters, describing the impact

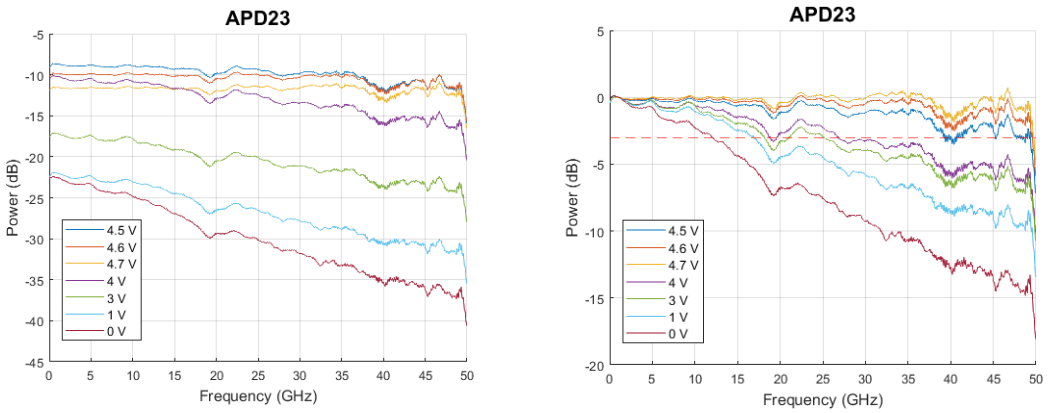

(a) Raw frequency response.

(b) Normalized frequency response.

Figure 3–9: Real S_{21} response of an APD at multiple bias points.

on the signal transmitted through the device. Responses are then normalized to a given frequency, often 1 GHz, and bandwidth is then measured at the 3 dB drop point. Figure 3–9 shows both normalized and non-normalized curves for different bias voltages.

We see that both the absolute amplitude of the signal as well as the roll off improves as bias increases for this particular device. In this case, the bandwidth is that of a vertical PD which is presented in greater details in the next section.

The impact of the following parameters on bandwidth has been studied through the aggregate test of over 100 PDs: Ge height, Ge width and Si width. The following are some broad takeaways from these measurements.

Germanium height. For VPIN design, the thinner germanium layer creates an increased E-field in silicon. Because of the higher field, more multiplication happens in Si, thus lowering the multiplication noise. Even though the smaller thickness

reduces the transit time compared to the normal process, it also increases the capacitance of the PD. We thus see lower initial bandwidth, but still a very strong performance at high gain. However, the lower germanium thickness also leads to a lower breakdown voltage as well as a reduced responsivity because there is simply less material to absorb the light.

Germanium width. A wider germanium layer has the obvious benefit of increasing absorption. We can see its impact by a higher initial responsivity. Figure 3–10 shows the impact of an increase of the Ge width by 25% on the responsivity. However, it also increases the RC constant, thus possibly lowering the bandwidth.

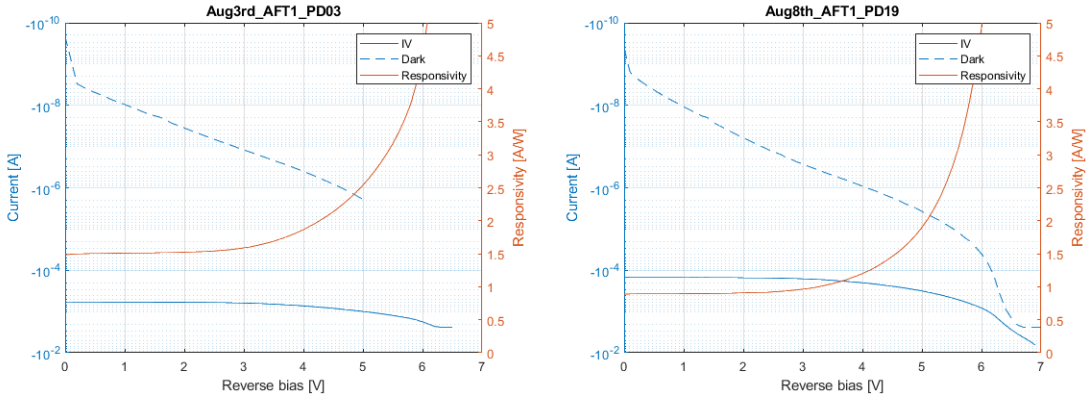

(a) 2.5 μm Ge width.

(b) 2 μm Ge width.

Figure 3–10: Comparison of current, responsivity and dark current for two APDs with a different Ge width.

Intrinsic silicon width. Again for the VPIN design variation with intrinsic Si, this parameter can have a significant impact on noise. It causes the E-field to have a higher intensity on the outer bands of the germanium. This reduces transit time and has a negligible impact ton the RC constant. However, this effect is most observed in the normal Ge thickness, and not in the thinner Ge layer. This suggests

that the thinner layer design is not transit time limited, compared to the normal design.

3.2.4 Transmission

Finally, large signal experiments are performed on the most promising PDs. This step consists of integrating the device of interest in a system of multiple optoelectrical components that mimic a real case use. The basic layout of such a system is presented in figure 3–11, and a more elaborate, real-world implementation is shown in figure 4–3. The high-level layout in this section shows the core components:

- A light source at telecommunication wavelengths
- A DAC capable of generating a pseudorandom binary sequence (PRBS)
- A modulator to transfer this electrical pattern to the light waves
- The PD under test
- A signal analyzer which will receive the signal from the PD and compare it with the original PRBS

With this setup, multiple parameters can be varied such as modulation format, bitrate, optical power and PD gain.

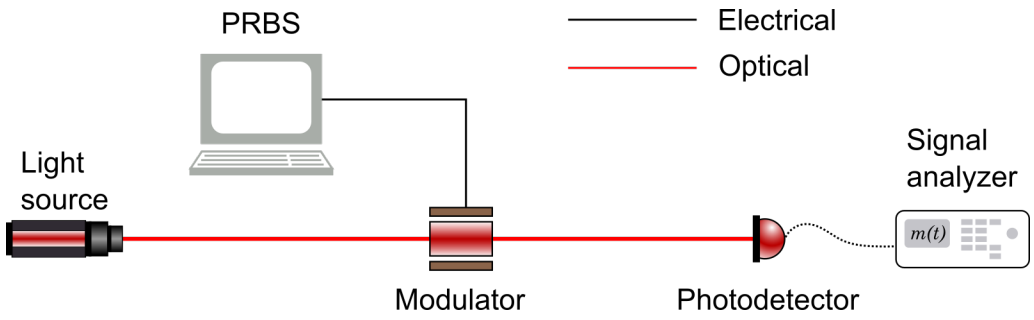

Figure 3–11: Simplified layout of a transmission measurement system.

CHAPTER 4
Results and Discussion

Over a hundred different devices were tested through various levels of scrutiny. In previous sections, major trends of design consideration impact on performance were presented. In this section, the specifics of top performing designs will be presented with details of performance. The first devices presented are two variations of a Ge-Si vertical P-I-N APD design with gain-bandwidths products of over 400 GHz operating in C-band with 28 Gb/s error free operation at -9 dBm input power [30]. Then, I will present a second pair of PDs with high transmission baud rates operating in O-band, the first of which is designed for 100 Gb/s applications with low excess noise, high gain and moderate bandwidth, while the second APD is designed for 400Gb/s applications with moderate gain and higher bandwidth [9].

4.1 High gain-bandwidth products

As previously presented, figure 3–1d shows the simplified cross section of both APD designs using a commercial process. The APDs were fabricated on two wafer splits in the same process on silicon-on-insulator wafers with a 220 nm think silicon layer and 2 μm thick buried oxide layer. Both APDs use a 2 μm wide, 15 μm long Ge as the absorption layer. The germanium epitaxy process was varied across the two wafer splits to obtain 400 nm and 200 nm germanium height h_{Ge}, referred to in this section as APD1 and APD2, respectively. The thinner Ge layer allows the electric field intensity to be higher and more concentrated in Si which enables the

impact ionization to happen in Si and decrease the APD excess noise [31], while the thicker Ge layer has better absorption of light. Further, a 500 nm wide intrinsic Si segment common to both designs is inserted under the Ge, to increase the electric field in the Si and improve noise performance of the APDs. Fig 3–3 also shows a sample layout of the APDs, where vertical shallow etched grating couplers (GCs) are used to couple light into the chip. Two outer GCs are used for calibration and alignment purposes, while the inner two GCs are used to couple light into the APDs and collect any unabsorbed light to characterize the absorption of the Ge.

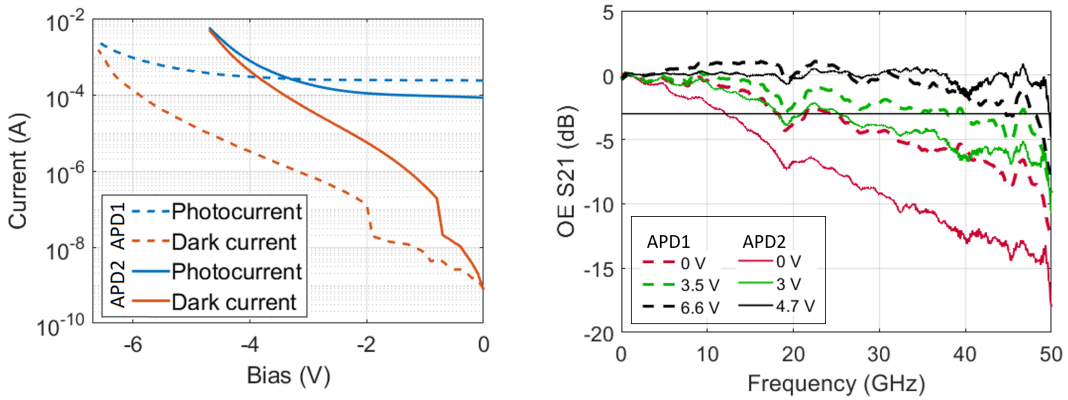

(a) (b)

Figure 4–1: a) IV curves of the two PD designs until breakdown with -5 dBm power input to the PD and b) small signal curves at different voltages for both APD designs, normalized at 1 GHz.

Figure 4–1a shows the dark current and the photocurrent of each APD for -5 dBm optical power into the APDs. The DC bias is applied to the APDs using a Bias Tee and a 50 GHz RF probe, and the current is measured using a picoammeter. The intrinsic responsivity of APD1 and APD2 at a wavelength of 1550 nm are measured to be 0.84 A/W and 0.33 A/W respectively. However, APD2 achieves higher gain

and lower breakdown voltages than the APD1 design. We observe two breakdown mechanisms for each APD. One mechanism due to high electric field, caused by increase bias voltage, and another due to heating effect as a result of high current running through the APDs. APD1 exhibits higher current capacity, due to the higher GE volume. OE small signal measurements were performed with an Agilent N4373D LCA and are presented in Fig 4–1b. Both APDs exhibit low bandwidths at low bias voltages, however significantly improve as the bias voltage increases even at higher gains; a phenomenon that is seen in Ge-Si APDs [32]. This is due to improvement in both transit time and capacitance at high reverse bias.

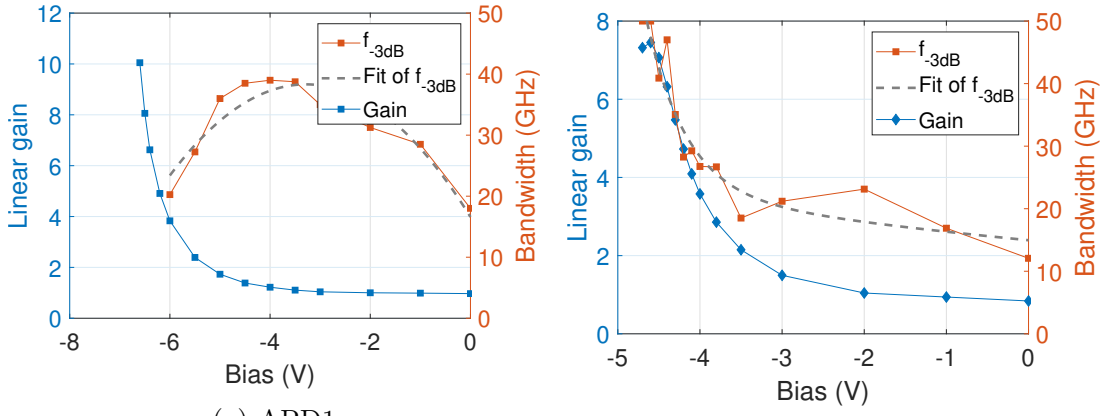

(a) APD1

(b) APD2

Figure 4–2: Gain and -3 dB OE bandwidth of both APDs from 0V bias until breakdown.

Figure 4–2 presents the gain as well as bandwidth achievable at various bias points for both PDs. The dip in bandwidth at -2V in figure 4–2a can be explained by the sensitivity of the measurement setup and the RF reflection that was present around 20 GHz as can be seen in 4–1b. The true BW at that bias point is closer to 30 GHz. This being said, we now see the different pattern between APD1 and APD2.

APD 2 experiences higher gain at lower voltages, but the total current capacity is higher for APD1. Furthermore, APD1 has a higher initial BW that increases slightly with gain until roughly 1.5X gain, but decreases sharply afterwards due to higher excess noise. APD2 however, with its thinner Ge layer, shows a lower initial BW but as gain increases its BW increases as well, to the 50 GHz limit of our measurement system. This shows a gain-bandwidth product in excess of 400 GHz.

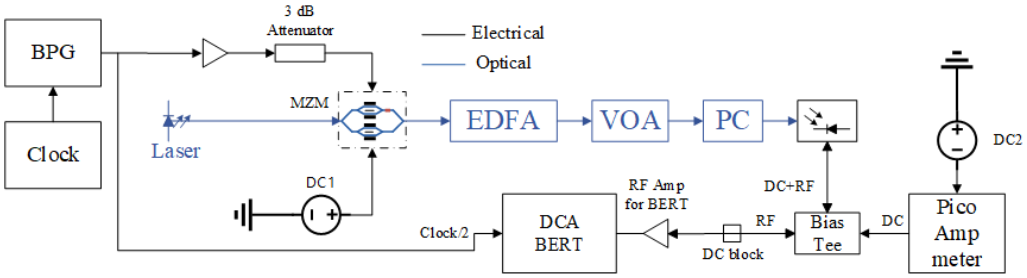

Figure 4–3: Experimental setup with electrical and optical path for DCA and BERT measurements.

Figure 4–3 shows the setup used to characterize the large signal performance of the APDs. We use a tunable C-band laser as input to a 30 GHz modulator. The modulator is driven by an SHF Bit Pattern Generator (BPG) using a $2^{31}-1$ pseudo-random-bit-sequence (PRBS) for On-Off Keying (OOK) modulation. A variable optical attenuator (VOA) is placed after the modulator to control the input power to the APDs and characterize its sensitivity. The DC bias is again applied to the APDs using a Bias Tee, and a 50 GHz GSG RF probe. The electrical output of the APDs is then connected to a bit error rate tester (BERT) to collect 1T bits for real time BER measurements and then to a digital communication analyzer (DCA) for

eye diagram measurements. To characterize the noise performance of the APD, we measure the SNR of the eye diagrams at various gains.

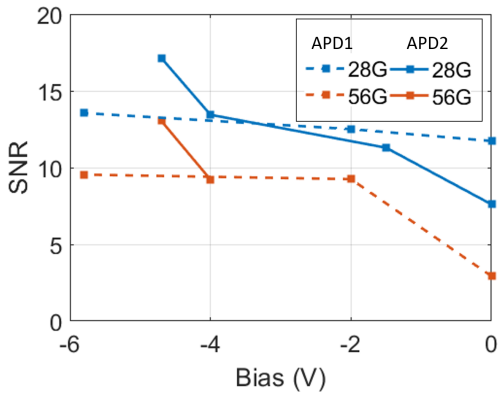

(a)

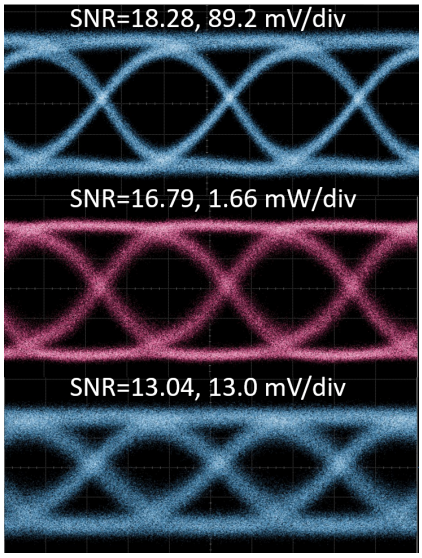

(b)

Figure 4–4: a) SNR variation with bias voltage for 0 dBm input power, b) Optical eyes of BPG (top), modulator (middle) and APD2 (bottom) at 56G and -4.7V bias and 0 dBm input power.

Fig 4–4a demonstrates the signal to noise ratio (SNR) improvements as reverse bias deepens. As shown, the SNR improves as the gain increases. However APD2 undergoes higher SNR increase at deeper bias due to higher gain, and better noise performance as a result of thinner Ge layer, and higher impact ionization happening in Si. Figure 4–4b, shows 56 Gb/s eye diagrams received at various points in the experimental setup: BPG (electrical), modulator (optical) and APD2 (electrical). Fig 4–5a shows the BER performance of the device for various optical powers at 28 Gb/s NRZ. We achieve error free performance ($< 10^{-12}$) at -9 dBm received power.

The BER of the APD for various bitrate at 4.7 V reverse bias and -5 dBm input power to the APD (gain of 7.5) is shown in figure 4–5b.

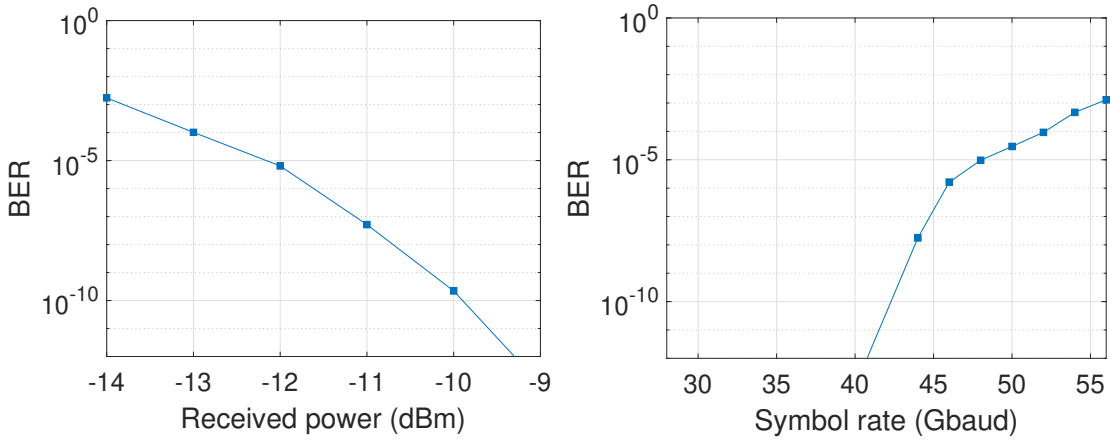

(a) (b)

Figure 4–5: a) BER versus received optical power at 28 Gbit/s NRZ and b) BER vs. bitrate for -5 dBm received optical power. Both refer to APD2.

As a deeper dive on signal degradation, we can look closer at the eye diagrams for various baud rates and reverse bias, as shown in figure 4–6. In our measurement setup, we don' measure SNR directly. Instead, we get the Q-factor, defined by equation (4.1) for NRZ signals.

$$Q = \frac{I_{\text{lvl1}} - I_{\text{lvl0}}}{\sigma_{\text{lvl1}} + \sigma_{\text{lvl0}}} \tag{4.1}$$

To convert the measured Q-factor into SNR, we use the relation presented in equation (4.2).

$$\text{SNR} = 10 \log_{10}(Q^2) \tag{4.2}$$

In figure 4–6 and table 4–1 we present the step-by-step view of signal degradation by sampling the signal at two different bitrates after the BPG, the modulator and the PD, for increasing bias voltages and both germanium thickness. By taking a close look, we see a few things. At 56 Gbps, we start to reach the bandwidth limit of the BPG and modulator, as rise and fall time are just short enough to cycle between 0 and 1 levels. We also see clearly the improvement in SNR out of the PD as we go into gain. As was shown with figure 4–2a, we also see that for the normal thickness Ge, going too deep into the avalanche region degrades the signal quality. However, the PD still provides a signal with much more amplitude, however more noisy (2V vs 6.2V bias). For the PD with a thin Ge layer, we only see SNR and amplitude improvement as we increase the reverse bias, until breakdown. We also see a 9-fold increase in eye amplitude at 28 Gbps between 1.5V and 4.75V reverse bias, which matches the gain measured with DC tests. Note that the normal Ge, 28 Gbps, 6.2V eye only looks dimmer because of equipment capture settings, not because of any degraded performance on the side of the PD.

Table 4–1: Values of SNR and eye amplitude for the PD eye diagrams presented in figure 4–6.

Type	Baud rate [Gbps]	Bias [V]	SNR	Amplitude [mV]
Normal Ge	28	0	11.73	5.70
		2.00	12.51	8.02
		6.20	11.89	23.05
Thin Ge	28	0	7.71	—
		1.5	10.45	2.38
		4.75	14.82	21.92
	56	1.50	3.86	—
		4.75	10.58	4.22

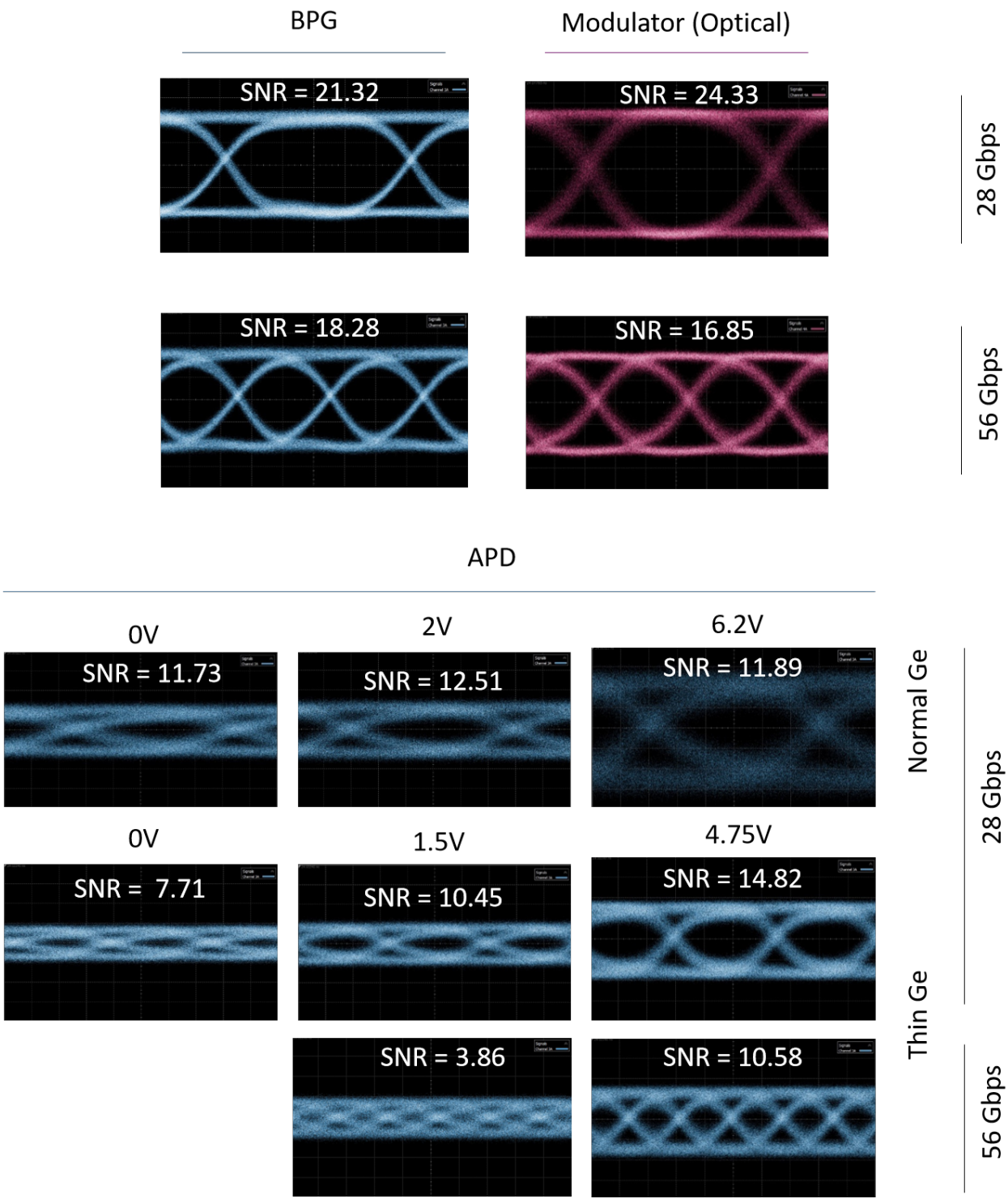

Figure 4–6: Matrix of eye diagrams for BPG, modulator and PD at multiple bias points and baud rates.

4.2 High data rates

Figure 3–2 and 3–1d shows the simplified cross section of the two APDs discussed in this section, referred to as APD3 and APD4, respectively. The first APD utilizes the SACM design presented earlier in earlier sections. To enhance the gain and bandwidth of this type of APD for the target bitrate of 25 Gb/s OOK without any DSP, several key design parameters were optimized, as discussed in section 3.2.3. The presented SACM APD utilizes a low-profile 200 nm height germanium, while the width and lengths of germanium are set at 1 μm and 15 μm respectively. The height of the germanium absorption layer is optimized to ensure the electric field strength in the germanium is strong enough for the generated carriers to reach saturation velocity and to ensure that all the light absorption is maximized. As a result, the design is optimized for a specific bandwidth and responsivity at gain of 1. Because of the low height of germanium, the impact ionization at higher bias voltages mostly happens in silicon, which results in a low excess noise performance of the APD. On the other hand, the second APD utilizes the SVPIN design discussed earlier. Similar to the SACM APD, this APD was fabricated with a germanium height of 200 nm, and width of 2.5 μm. The silicon intrinsic width is set to 500 nm.

Figure 4–7 presents the photocurrent and responsivity of each APD. The DC bias is applied to the APDs using a Bias Tee, and a multi-needle DC probe. The output current of the APD is then monitored using a picoammeter. A 3-dB splitter is used to divide the tunable laser output into two, the outputs of the splitter are then applied to GC 1 to monitor the power into the APD and GC 2 for input to the APD. GC 3 is used to monitor the unabsorbed light from the APD and characterize

the absorption profile of the APD. The SACM responsivity curve can be divided in to three stages: a) from 0 to -7.5 V, the electric field in the Ge is not strong enough to collect all the electron hole pair as a result the responsivity increases as the voltage increases, b) from -7.5 to -11 V the responsivity is relatively flat, as the electric field is strong enough for the carrier to reach saturation velocity, we consider responsivity at -10 V as gain 1, and c) below -11 V, where the impact ionization starts and the avalanche process begins. On the other hand, the vertical P-IN APD reaches the necessary electric field strength for saturation velocity and impact ionization at noticeably lower voltages due to is structure and doping stack.

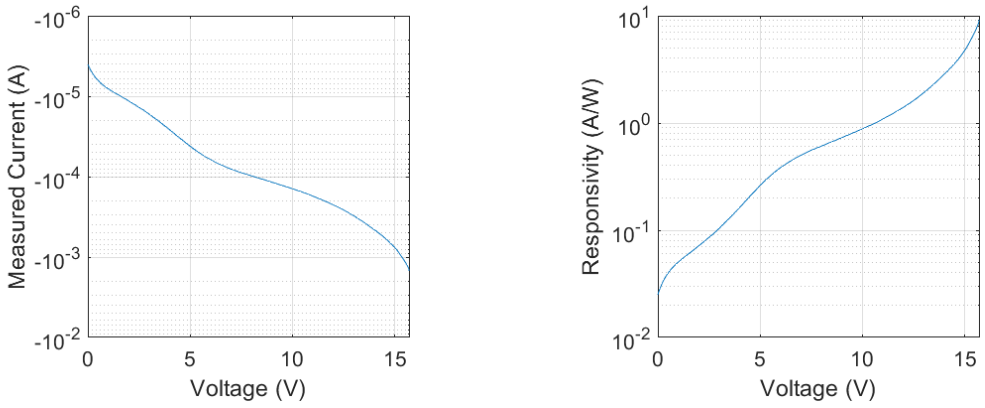

Figure 4–7: Current and responsivity of APD3 in O-band, -8 dBm power reaching the PD.

Figure 4–9 presents the large signal experimental setup, similar to the setup in figure 4–3, but presented again here to accurately portray the setup for this experiment. A tunable O-band laser is used as input to a 40 GHz LiNbO3 modulator. The modulator is driven by a $2^{31}-1$ PRBS generated using the SHF bit pattern generator

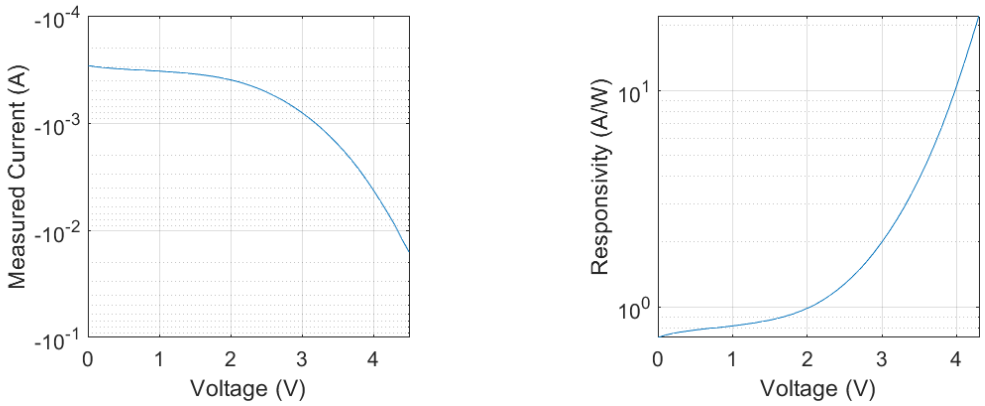

(a) (b)

Figure 4–8: Current and responsivity of APD4 in O-band, -4 dBm power reaching the PD.

(BPG) for On-Off Keying (OOK) modulation and without use of any digital signal processing (DSP), while an 8 bit, 88 GSample/s digital to analog converter (DAC) is used for OOK and PAM-4 with DSP. Vertical shallow etched grating couplers are used to couple the modulated light in the SiP chip. A variable optical attenuator (VOA) is placed after the modulator to control the input power to the APDs and characterize the sensitivity of the APDs. The DC bias is applied to the APDs using a Bias Tee, and a 40 GHz GSG RF probes. The RF received signal of the APDs is then connected to an error detector for real time BER measurements. For PAM-4 modulation, a real time oscilloscope (RTO) is used to capture the signal and perform offline error counting.

The transmitter DSP includes: symbol generation, pulse shaping for symbol rates lower than 88 Gbaud, RF spectral pre-compensation filter, clipping, and quantization. The signal is then amplified to 5 Vpp and is applied to the modulator. The

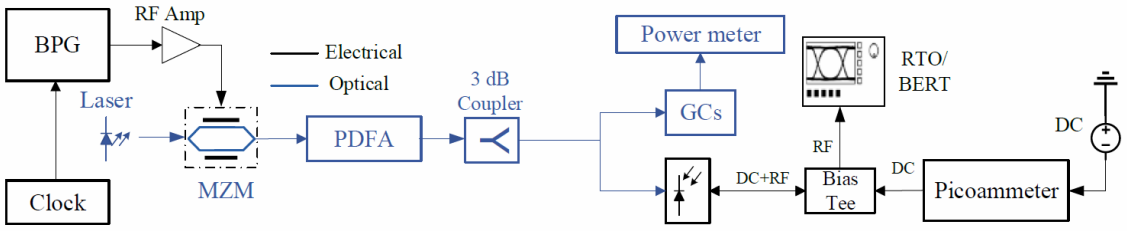

Figure 4–9: Experimental transmission setup.

receiver DSP consists of: sampling the received signal at 160 GSample/s, matched filtering, clock recovery, receiver equalization and symbol decision.

Figure 4–10 presents OE small signal measurements of both APDs. The measurements are done using a 50 GHz Keysight Lightwave Component Analyzer (LCA). At low bias voltages the SACM has an extremely low 3-dB bandwidth. This is because of the low electric field intensity inside germanium. As a result, the generated electron-hole pairs do not reach the saturation velocity, and the bandwidth is limited by the long transit time. As the bias voltage increases, the transit time is lowered, and the bandwidth is improved. On the other hand, the electric field intensity in germanium in the vertical P-I-N APD is strong and the APD is not limited by the transit time. The Vertical APD has over 40 GHz of bandwidth at -4 V bias which is the limit of the RF probes, while at -4.2 the bandwidth of the APD is above 30 GHz.

Next, we examine the BER performance of each APD using a SHF bit error rate tester (BERT) for OOK modulation. 6 Tbits are collected using the BERT and error counting is done in real time, as a result we can report BER values below 10^{-12}. For PAM-4, a 63 GHz RTO is used to capture the APD output. The signal is sampled

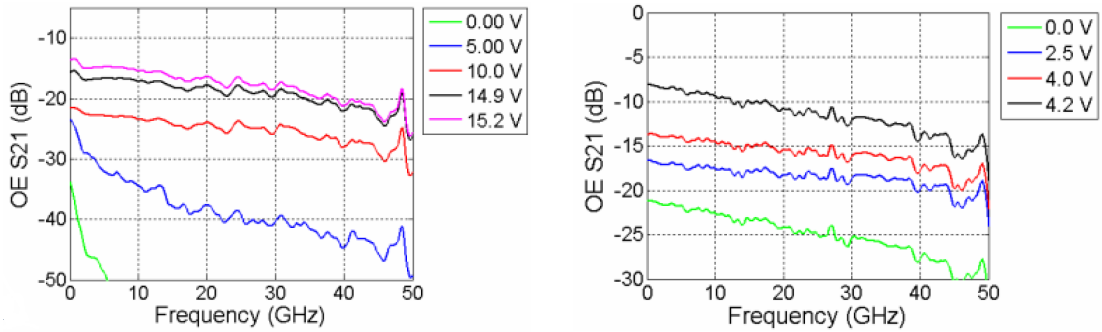

(a) (b)

Figure 4–10: OE small signal measurements of the a) APD3 and b) APD4.

at 160 GSample/s and stored for the offline receiver DSP. Fig. 4–11 presents the BER performance of each APD for various baud rates and modulation formats. The red dotted lines on the graphs note the KP4 hard-decision, FEC threshold, at 2.4 × 10-4 and the hard decision (HD) FEC threshold 3.8 × 10-3 for reference, which is commonly referred to in recent papers.

Figure 4–11 shows that both APDs achieve error free 25 Gbaud OOK transmission without any DSP used. The SACM has slightly higher sensitivity and operates error free with -12 dBm input power while the vertical P-I-N APD can achieve higher baudrate. This is due to the higher bandwidth of the vertical APD. Further we achieve 88 Gbaud OOK and 56 Gbaud PAM-4 below KP4 FEC threshold.

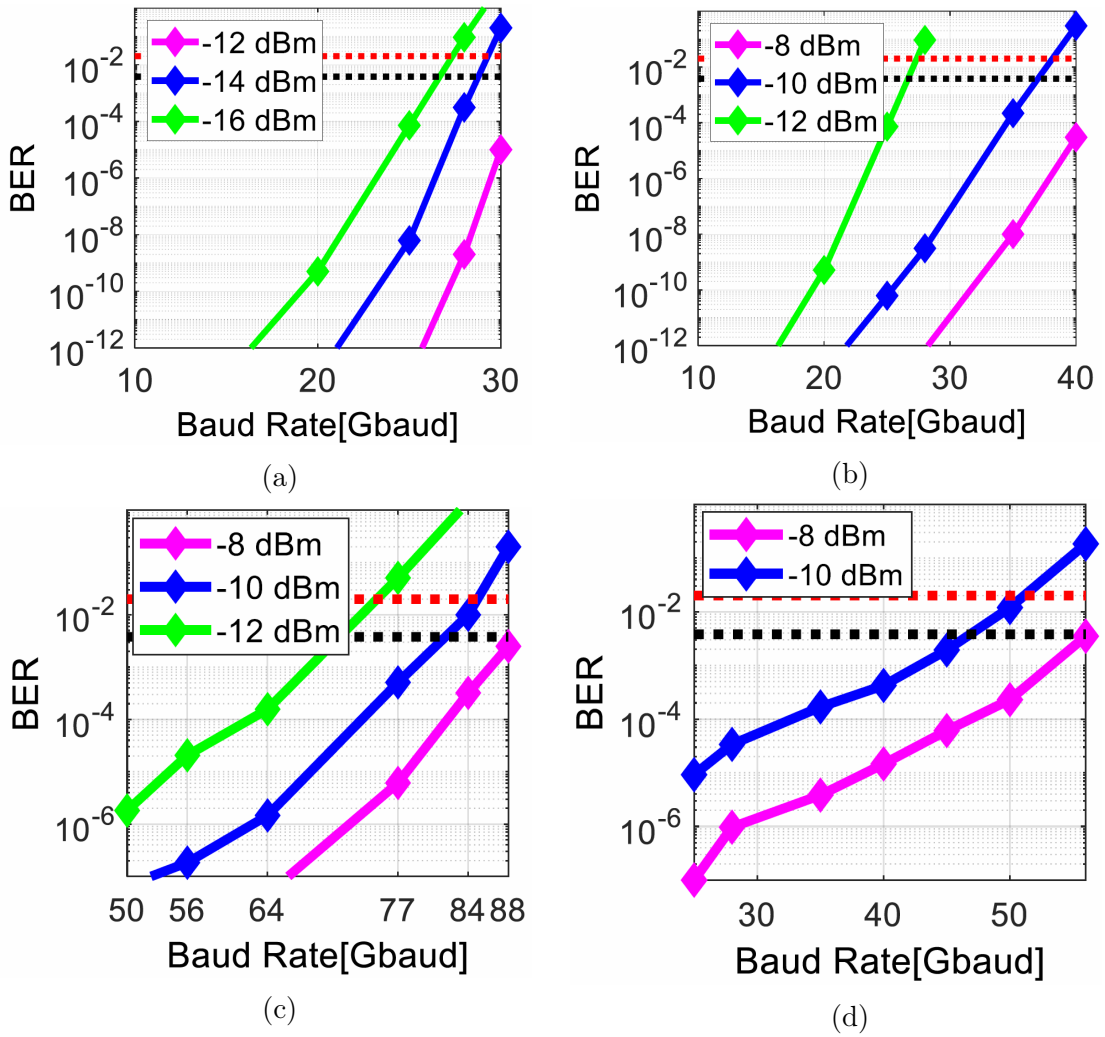

Figure 4–11: BER performance vs. baudrate for a) OOK with APD3 at -14.90 V bias, b) OOK APD4 without DSP at -3.95 V bias, c) OOK APD4 with DSP at -3.95 V and d) PAM-4 APD4 at -3.95 V bias.

CHAPTER 5
Tool development

To facilitate data processing and invest in future measurement capabilities, a variety of tools and techniques were developed. These tools offer a significant platform for future work on the development of SiGe PDs and deserve to be outlined in this section. The major contributions are outlined in the following sections.

5.1 LCA Viewer

The LCA Viewer program is an easy to use tool to process small signal measurement data. The tool takes S-parameter files in an `.s2p` format, which provides S_{11}, S_{12}, S_{21} and S_{22} data. By pointing to a folder that contains multiple sub-folder of individual device measurements, the viewer provides a dynamic list that updates with available traces for each bias point that was measured. A single or multiple traces can then be plotted. The traces can then be normalized at a specified frequency to easily extract the 3 dB bandwidth. A rolling average can also be applied to smooth ripples in the curve. These graphs can be viewed dynamically: zoomed in and inspected point by point. A copy of the figure can then be exported. This workflow greatly improves on the previous methods of exploring LCA data, which was an ad-hoc mix of screen captures and one-offs Matlab scripts. This tool can be used for any other device where small signal data is measured at various bias points, such as modulators. The default setting is to plot the real component of the

S21 curve, but real and complex values for all S parameters are also accessible. The graphical user interface in a typical use case can be seen in figure 5–1.

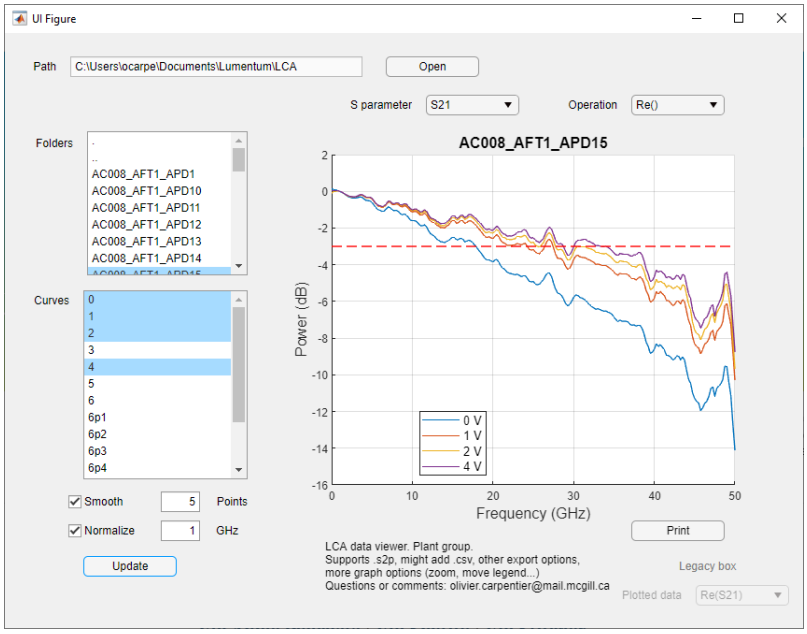

Figure 5–1: S-parameter analysis application.

5.2 PD data processing

A different tool was developed to process raw DC measurement data. By providing the user prompts to select desired data to analyse as well as to identify critical parts of a curve, this tool provides fast, reliable and consistent analysis, reducing human variation in processing the data.

The logical sequence of operations is shown in figure 5–2. We initially extract raw data for GC calibration, dark and photocurrent. Data is then cleaned up and if the input laser power is not provided, it is extracted from metadata. Prompts ask the user to identify the normal operation region (where gain is 1) and where the measurements end, whether because it has reached the maximum bias point,

because the PD broke down or because the bias source had reached its compliance level. Parameters are then derived such as gain and responsivity, which can then be exported along with the original data.

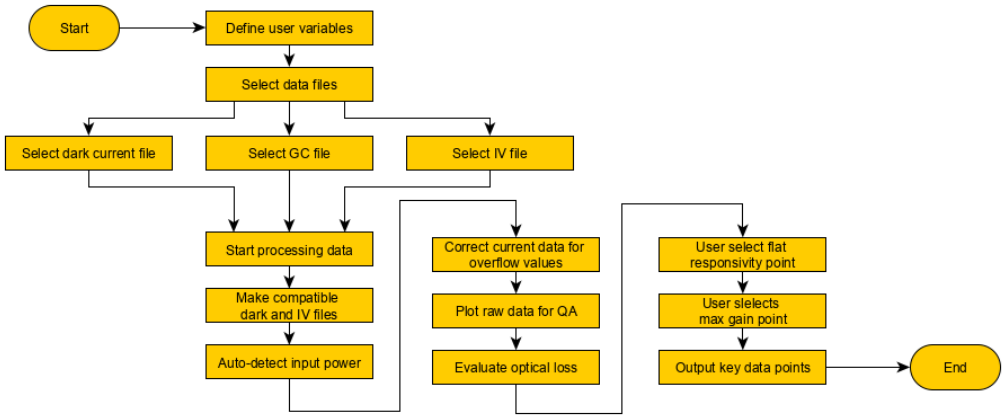

Figure 5–2: Process flow for DC data processing.

5.3 Data aggregation

By having a standardized and efficient way of processing large amounts of DC and small signal data, we were able to create a dashboard with a single view providing all the necessary data to analyze the impact of design variations on each type of PD design. This reporting method also allows to slice available data by their physical values, such as geometric parameters, current density and more. A view is presented in figure 5–3.

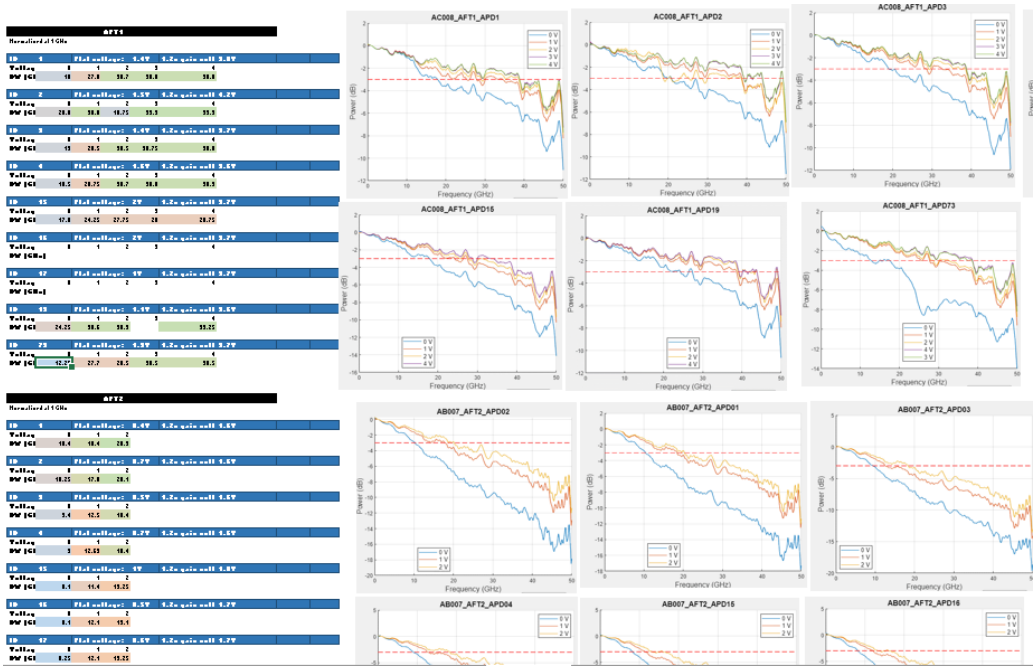

Figure 5–3: Dashboard view of DC and EO measurement results.

CHAPTER 6
Conclusion

6.1 Summary

As demand for connectivity grows and economic pressure pushes for ever more efficient and closely integrated networking devices, the benefits of silicon photonics become increasingly attractive. By carefully engineering the materials and geometry of photodetectors, it is possible to push the performance of SiGe APDs to new heights.

In chapter 3, I outlined a standardized testing and measurement methodology for dark and photocurrent as well as small signal and data transmission performance. I also discussed how certain design parameters affect each performance characteristic.

In chapter 4, I presented two different milestones. First, we present an APD vertical design capable of 28 Gbit/s error free operation with -9 dBm input power as well as a gain-bandwidth product > 400 without any DSP. Second, we report 25 Gb/s error free operation with -12 dBm input power without the use of any DSP using the SACM APD. Additionally, 112 Gb/s PAM-4 operation below the KP4 forward error correction (FEC) threshold of 2.0×10^{-4} using the vertical P-I-N APD with -8dBm input power was achieved which, to the best of our knowledge at the time, was the highest reported bitrate using an APD on SiP platform.

6.2 Future Work

In this work, I have focused on evaluating the raw performance of APDs through multiple design variations as well as establishing a standardized and reproducible method of testing. By leveraging the leanings from my thesis, I will present three paths for future work.

Simulation. Access to experimental data is an important part of validating theoretical models. By extracting further parameters from the experimental data and performing more metrology measurements, it would be possible to improve on models to more closely match reality. For example, multiple models use bulk material properties. However, the lattice mismatch between Si and Ge as well as the addition of vias and doping in a thin, 200 nm layer of Ge leads to specific performance characteristics. Having access to a trusted optical model and equivalent small-signal circuit that take into account some of the more edge-case characteristics and is shown to closely match real-world performance would be a great tool for APD development.

Integration. The measurements performed in this work were all done on stand-alone PDs that were GC coupled and electrically probed. This setup is great to test a large volume of PDs, but doesn't match the operation environment that is intended for the PD. By moving further in the integration stack of a complete ROSA, it will be possible to better assess the performance of a PD in a real-world setting. This could means testing the PDs in a PIC coupled with ECs, multiple wavelengths that are demultiplexed on-chip and wire-bonded electrical contacts.

Performance. Even though the PDs tested have shown some impressive performance, it is still possible to push the envelope even further. By using state of the

art DACs and DSP or by using inductive peaking to extend the bandwidth of PDs, it would be possible to achieve- higher performance metrics.

References

[1] Elisabetta Nocerino. *The Semiconductor Multiplication System for Photoelectrons in a Vacuum Silicon Photomultiplier Tube and Related Front End Electronics*. PhD thesis, 11 2016.

[2] Research And Market. Hyperscale Data Center - Global Market Outlook (2017-2023). Technical report, Research And Markets, 2017.

[3] Cisco. Cisco Global Cloud Index: Forecast and Methodology (2016-2021). Technical report, Cisco, San Jose, California, 2018.

[4] R Soref and B Bennett. Electro-optical effects in ferroelectrics. *IEEE Journal of Quantum Electronics*, QE-23(1):123–129, 1987.

[5] H Melchoir, M Fisher, and F Arams. Photodetectors for Optical Communication. *Journal of Optical Communications*, 58(10):1466–1486, 1970.

[6] Winnie N. Ye and Yule Xiong. Review of silicon photonics: History and recent advances. *Journal of Modern Optics*, 60(16):1299–1320, 2013.

[7] Yimin Kang, Han Din Liu, Mike Morse, Mario J. Paniccia, Moshe Zadka, Stas Litski, Gadi Sarid, Alexandre Pauchard, Ying Hao Kuo, Hui Wen Chen, Wissem Sfar Zaoui, John E. Bowers, Andreas Beling, Dion C. McIntosh, Xiaoguang Zheng, and Joe C. Campbell. Monolithic germanium/silicon avalanche photodiodes with 340GHz gain-bandwidth product. *Nature Photonics*, 3(1):59–63, 2009.

[8] Christopher T. DeRose, Douglas C. Trotter, William A. Zortman, Andrew L. Starbuck, Moz Fisher, Michael R. Watts, and Paul S. Davids. Ultra compact 45 GHz CMOS compatible Germanium waveguide photodiode with low dark current. *Optics Express*, 19(25):24897, 2011.

[9] Alireza Samani, Olivier Carpentier, Eslam El-fiky, Maxime Jacques, Amar Kumar, Yun Wang, Claude Gamache, Ping-chiek Koh, and David V Plant. Highly Sensitive , 112 Gb / s O-band Waveguide Coupled Silicon-Germanium Avalanche

Photodetectors. *2019 Optical Fiber Communications Conference and Exhibition (OFC)*, pages 1–3, 2019.

[10] Mengyuan Huang, Su Li, Pengfei Cai, Guanghui Hou, Tzung I. Su, Wang Chen, Ching Yin Hong, and Dong Pan. Germanium on silicon avalanche photodiode. *IEEE Journal of Selected Topics in Quantum Electronics*, 24(2), 2018.

[11] Binhao Wang, Zhihong Huang, Xiaoge Zeng, Di Liang, Wayne V Sorin, and Raymond G Beausoleil. 60 Gb / S Pam4 Low-Voltage Waveguide Si-Ge Avalanche Photodiode. *Ecoc*, 1(c):3–6, 2019.

[12] Stefan Lischke, Dieter Knoll, Christian Mai, Lars Zimmermann, Anna Peczek, Marcel Kroh, Andreas Trusch, Edgar Krune, Karsten Voigt, and A. Mai. High bandwidth, high responsivity waveguide-coupled germanium p-i-n photodiode. *Optics Express*, 23(21):27213, 2015.

[13] S. Lischke, D. Knoll, C. Mai, M. Kroh, D. Schmidt, A. Peczek, J. Kreisl, J. M. Lee, M. Kim, W. Y. Choi, and L. Zimmermann. Design effects on the performance of high-speed Ge photo detectors. *IEEE International Conference on Group IV Photonics GFP*, 2016-Novem:22–23, 2016.

[14] Joseph W Goodman. Optical interconnects for vlsi system. *Proc. IEEE*, 72:159–174, 1984.

[15] Guoqing Chen, Hui Chen, Mikhail Haurylau, Nicholas Nelson, David Albonesi, Philippe M. Fauchet, and Eby G. Friedman. Electrical and optical on-chip interconnects in scaled microprocessors. *Proceedings - IEEE International Symposium on Circuits and Systems*, pages 2514–2517, 2005.

[16] Solomon Assefa, Fengnian Xia, S. W. Bedell, Ying Zhang, Teya Topuria, Philip M. Rice, and Yurii A. Vlasov. CMOS-integrated small-capacitance germanium waveguide photodetector for optical interconnects. *Optics InfoBase Conference Papers*, pages 10–12, 2009.

[17] Solomon Assefa, Fengnian Xia, and Yurii A. Vlasov. Reinventing germanium avalanche photodetector for nanophotonic on-chip optical interconnects. *Nature*, 464(7285):80–84, 2010.

[18] Jacob S Levy, Alexander Gondarenko, Mark A Foster, Amy C Turner-Foster, Alexander L Gaeta, and Michal Lipson. Cmos-compatible multiple-wavelength oscillator for on-chip optical interconnects. *Nature photonics*, 4(1):37–40, 2010.

[19] Chen Sun, Mark T. Wade, Yunsup Lee, Jason S. Orcutt, Luca Alloatti, Michael S. Georgas, Andrew S. Waterman, Jeffrey M. Shainline, Rimas R. Avizienis, Sen Lin, Benjamin R. Moss, Rajesh Kumar, Fabio Pavanello, Amir H. Atabaki, Henry M. Cook, Albert J. Ou, Jonathan C. Leu, Yu Hsin Chen, Krste Asanović, Rajeev J. Ram, Miloš A. Popović, and Vladimir M. Stojanović. Single-chip microprocessor that communicates directly using light. *Nature*, 528(7583):534–538, dec 2015.

[20] IEEE 802.3 Ethernet Working Group, 2020. http://www.ieee802.org/3/.

[21] Erman Timurdogan, Zhan Su, Ren Jye Shiue, Matthew J. Byrd, Christopher V. Poulton, Kenneth Jabon, Christopher Derose, Benjamin R. Moss, Ehsan S. Hosseini, Ivan Duzevik, Michael Whitson, Ronald P. Millman, Dogan A. Atlas, and Michael R. Watts. 400G Silicon Photonics Integrated Circuit Transceiver Chipsets for CPO, OBO, and Pluggable Modules. *2020 Optical Fiber Communications Conference and Exhibition, OFC 2020 - Proceedings*, 1:17–19, 2020.

[22] Monireh Moayedi Pour Fard, Glenn Cowan, and Odile Liboiron-Ladouceur. Responsivity optimization of a high-speed germanium-on-silicon photodetector. *Optics Express*, 24(24):27738, nov 2016.

[23] Andrea De Iacovo, Andrea Ballabio, Jacopo Frigerio, Lorenzo Colace, and Giovanni Isella. Design and Simulation of Ge-on-Si Photodetectors With Electrically Tunable Spectral Response. *Journal of Lightwave Technology*, 37(14):3517–3525, 2019.

[24] Lukas Chrostowski and Michael Hochberg. *Silicon photonics design*. Cambridge University Press, 2015.

[25] Ross Anthony, David E. Hagan, Dylan Genuth-Okon, Laura Martinez Maestro, Iain F. Crowe, Matthew P. Halsall, and Andrew P. Knights. Extended Wavelength Responsivity of a Germanium Photodetector Integrated with a Silicon Waveguide Exploiting the Indirect Transition. *IEEE Journal of Selected Topics in Quantum Electronics*, 26(2), 2020.

[26] G Margaritondo, N. G. Stoffel, and A. D. Katnani. Microscopic Investigation of the Band Discontinuities at the Silicon-Germanium Heterojunction Interface. *Solid State Communications*, 36(lll):1–22, 1980.

[27] Xuewei Zhao, M. Moeen, M. S. Toprak, Guilei Wang, Jun Luo, Xingxing Ke, Zhihua Li, Daoqun Liu, Wenwu Wang, Chao Zhao, and Henry H. Radamson.

Design impact on the performance of Ge PIN photodetectors. *Journal of Materials Science: Materials in Electronics*, 31(1):18–25, 2020.

[28] Xiaogang Bai, Ping Yuan, Paul McDonald, Joseph Boisvert, James Chang, Rengarajan Sudharsanan, Michael Krainak, Guangning Yang, Xiaoli Sun, Wei Lu, Zhiwen Lu, Qiugui Zhou, Wenlu Sun, and Joe Campbell. Development of low excess noise SWIR APDs. In Bjørn F. Andresen, Gabor F. Fulop, and Paul R. Norton, editors, *Infrared Technology and Applications XXXVIII*, volume 8353, pages 878 – 884. International Society for Optics and Photonics, SPIE, 2012.

[29] Han Din Liu, Huapu Pan, Chong Hu, Dion McIntosh, Zhiwen Lu, Joe Campbell, Yimin Kang, and Mike Morse. Avalanche photodiode punch-through gain determination through excess noise analysis. *Journal of Applied Physics*, 106(6):1–5, 2009.

[30] Olivier Carpentier, Alireza Samani, Maxime Jacques, Eslam El-fiky, Yun Wang, Ping-chiek Koh, Nicolas Abadia Calvo, and David Plant. High Gain-Bandwidth Waveguide Coupled Silicon Germanium Avalanche Photodiode. *Cleo*, 2019.

[31] C Hu, K A Anselm, B G Streetman, and J C Campbell. Excess Noise in GaAs Avalanche Photodiodes with Thin Multiplication Regions. 33(7):1089–1093, 1997.

[32] Srinivasan Ashwyn Srinivasan, Peter De Heyn, Gaspard Hiblot, Hongtao Chen, Sebastien Lardenois, Marianna Pantouvaki, and Joris Van Campenhout. Silicon-contacted waveguide integrated Ge / Si avalanche photodiode with 32 GHz bandwidth and multiplication gain > 8. pages 2–4.